Title

Tuning the Optical Absorption Edge of Vacancy-Ordered Double Perovskites through Metal Precursor and Solvent Selection

Journal

Chemistry of Materials, 36(19)

ISSN

0897-4756 1520-5002

Authors

Brumberg, Alexandra

Kuklinski, Owen

Kent, Greggory T

et al.

Publication Date

2024-09-16

DOI

10.1021/acs.chemmater.4c01701

Peer reviewed

Tuning the Optical Absorption Edge of Vacancy-Ordered Double Perovskites through Metal Precursor and Solvent Selection

Alexandra Brumberg[1,2], Owen Kuklinski[1], Greggory T. Kent[1,2], Emily E. Morgan[1,2], Alexander A. Mikhailovsky[3], T. Amanda Strom[2], Michael L. Chabinyc[1,*], and Ram Seshadri[1,2,*]

[1] Department of Materials, University of California, Santa Barbara, CA 93106, United States

[2] Materials Research Laboratory, University of California, Santa Barbara, CA 93106, United States

[3] Department of Chemistry, University of California, Santa Barbara, CA 93106, United States

Abstract

Vacancy-ordered double perovskites with the formula A_2MX_6 (where A is a +1 cation, M is a +4 metal, and X is a halide ion) offer improved ambient stability over other main-group halide AMX_3 perovskites and reduced toxicity compared to those containing lead. These compounds are readily formed through a number of synthetic routes; however, the manner in which the synthetic route affects the resulting structure or optoelectronic properties has not been examined. Here, we investigate the role of distinct precursors and solvents on the formation of the indirect band gap vacancy-ordered double perovskite Cs_2TeBr_6. While Cs_2TeBr_6 can be synthesized from $TeBr_4$ or TeO_2, we find that synthesis from $TeBr_4$ is more sensitive to solvent selection, requiring a polar solvent to enable the conversion of $TeBr_4$. Synthesis from TeO_2 can proceed in any organic solvent, provided that HBr is added to solubilize TeO_2 and enable the formation of $[TeBr_6]^{2-}$. Furthermore, the choice of metal precursor and solvent impacts the product color and optical absorption edge, which we find arises from particle size effects. The emission energy remains unaffected, consistent with the idea that emission in these zero-dimensional structures arises from the isolated $[TeBr_6]^{2-}$ octahedra, which undergo dynamic Jahn-Teller distortion, rather than band-edge recombination. Our work highlights how even minor changes in synthetic procedures can lead to variability in metrics such as the absorption edge and emission lifetime and sheds light

into how the optical properties of these semiconductors can be controlled for light-emitting applications.

Introduction

Metal halide perovskites have garnered significant research interest in recent years, not only as photovoltaics but also as light-emitting diodes (LEDs), lasers, and sensors.[1,2] In this regard, vacancy-ordered double perovskites (VODPs) of the formula A_2MX_6 (where A is a +1 cation, M is a +4 metal, and X is a halide) stand out as attractive candidates for light-emitting applications[3–6] owing to their improved stability[7,8] in light and air compared to AMX_3 formulations and their highly Stokes shifted, broad emission.[9,10] This broad emission makes them particularly well-suited for single-component white light generation, such that it is of great interest to understand the origin of this unusual emission.[10–12]

The optical, electronic, and environmental properties of VODPs are a result of a structure (**Figure 1a**) in which half of the MX_6 octahedra of the AMX_3 structure have been replaced with vacancies and the M^{2+} metal centers have been replaced with M^{4+} cations that are more stable against oxidation.[13] The MX_6 octahedra behave as relatively isolated $[MX_6]^{2-}$ clusters that can be analyzed *via* the lens of molecular orbital theory. The X = Cl compounds feature the flattest band dispersion,[14] corresponding to the most molecular-like bonding. As the ionic radius and softness of the halide increases from Cl < Br < I, the molecular nature of the bonding is reduced, concomitant with an increase in dispersion band curvature and a decrease in both the electron and hole effective masses.[14,15] While the molecular picture of bonding in the $[MX_6]^{2-}$ clusters can aid in understanding the photophysical properties of these compounds, there is a need to unify this molecular model with one for solid-state systems.

The isolated nature of the coordinated metal octahedra in the VODP structure also means that they are prone to deformation, even more so than the conventional AMX_3 perovskite structure.[16,17] This renders VODPs amenable to the formation of polarons, whereby following photoexcitation, coupling of charge carriers (*i.e.* electrons or holes) or excitons to phonons induces structural deformation.[18] If electron- or exciton-phonon coupling is strong enough, the structural deformation will be highly localized, creating a potential well that inhibits carrier or exciton motion. The latter results in a highly localized exciton known a self-trapped exciton.[16–19] Emission from the self-trapped exciton state occurs at a lower energy than excitation and is highly broadened, consistent with the type of emission observed in VODPs. While the mechanism of self-trapped exciton emission is consistent with the nature of VODPs, the challenge of directly probing excited state geometries makes it difficult to confirm self-trapped exciton formation.

Within the large compositional space of VODPs, most research thus far has focused on VODPs containing Ti^{4+}, Zr^{4+}, or Sn^{4+}, which are direct band gap and contain no valence electrons, or Te^{4+}, which is indirect gap and contains a $5s^2$ lone pair.[13,20–22] The ns^2 lone pair is suspected to play a role in a number of optoelectronic processes, including enhanced emission[23–25] and nonlinear harmonic generation.[26–28] In particular, spin-orbit coupling and dynamic Jahn-Teller distortion enhance formation of and emission from the triplet state, which closely resembles the self-trapped exciton emission that is suspected to be the origin of the broad and highly Stokes-shifted emission in all VODPs.[29,30] In the case of Te-based VODPs, both triplet and self-trapped exciton emission are possible, making it difficult to distinguish the origin of emission and understand how the $5s^2$ lone pair affects an already perplexing emission mechanism.

Unraveling the origin of emission in a semiconductor requires samples whose structures are well understood, so that factors that can confound emission mechanisms—such as defects—are accounted for. The large negative formation energies[7,31] of VODPs make them relatively straightforward to synthesize and have led to the development of several synthetic strategies, including hydrothermal, microwave, solid state, and solution synthesis techniques.[6,32–38] Despite this flexibility, relatively few reports have investigated the effect of synthetic strategy on the resulting perovskite structure,[6,39] as all of the aforementioned approaches result in the intended phase-pure compound. However, reports from the perovskite literature suggest that many synthesis and processing conditions actually do affect characteristics such as defect formation, metal-solvent complexation, strain, and phase impurities.[40–45] Even when these factors do not impede the formation of a phase-pure product, they can have significant implications on electronic structure that thereby affect optoelectronic properties such as absorption onset,[46–48] photoluminescence quantum yield,[49,50] and carrier transport.[48,50] For VODPs in particular, there is a variation in reported band gaps, with experimental values for Cs_2SnI_6 ranging from 1.25 to 1.35 eV for powders[22,51–53] and 1.26 to 1.63 eV for films,[8,46,54–57] compared to 0.88 to 1.48 eV predicted by density functional theory using different levels of theory.[22,48,52,58,59] Within one paper alone, band gaps ranging between 1.28 and 1.41 eV were reported for Cs_2SnI_6 depending on the amount of CsI impurity present in the film.[46] The change in optical absorption is consistent with the *n*-type nature of Cs_2SnI_6, wherein iodide vacancies and interstitial tin defects manifest as *n*-type dopants and an apparent band gap modification.[22,51,60] This highlights the need to understand the nature of defects across all VODPs to enable consistent and reproducible sample production and on-demand manipulation of electronic properties.

Here, we investigate the relationship between synthesis, structure, and optical properties by synthesizing Cs_2TeBr_6 from two different precursors ($TeBr_4$ and TeO_2) and in a variety of different solvents. We find that nearly all of the synthetic conditions attempted here result in Cs_2TeBr_6 powders that are phase-pure by powder X-ray diffraction. However, the color of the powders varies, which is consistent with UV-vis absorption spectra that reveal different absorption onsets for the different powders. Despite these differences in absorption, the compounds have identical optical emission spectra, with emission occurring at the same energy but with different decay lifetimes. Scanning electron microscopy (SEM) suggests that these optical differences can be ascribed to particle size differences rather than intrinsic structural differences. Based on these results, we offer that synthesis with different Te precursors and in different solvents affects the resulting defect density through solvent coordination during synthesis. Our results demonstrate a useful route towards tuning optical absorption and emission properties while also addressing the band gap reproducibility issue in the field of VODPs.

Methods

Chemicals: Chemicals were purchased from the following vendors: *Alfa Aesar*: cesium bromide (99% metal basis); *Fisher Chemical*: ethanol (anhydrous, histological grade), ethyl acetate (certified ACS grade); *Lab Chem:* isopropyl alcohol (ACS grade); *Sigma-Aldrich*: acetonitrile (anhydrous, 99.8%), methanol (HPLC grade, ≥99.9%), tellurium dioxide (99.995% trace metals basis); *Spectrum Chemical MFG Corp*: hydrobromic acid (technical grade, 48%); *Thermo Scientific*: methyl acetate (99%), tellurium(IV) bromide (99.9% metals basis). All chemicals were used as received, except for cesium bromide, which was dried overnight in an oven at 120 °C to remove excess moisture.

Synthesis of Cs_2TeBr_6 from $TeBr_4$: In a 20 mL scintillation vial, 0.25 mmol (112 mg) $TeBr_4$ was dissolved in 6 mL of a chosen solvent by stirring and heating to ~60 °C on a magnetic hot plate. Upon complete dissolution of the yellow powder, 0.5 mmol CsBr (106 mg) was directly added to the solution as a solid (see **Figure S1** and associated discussion). The reaction was allowed to proceed for the desired reaction time under stirring (1 hr in methanol or 2 hrs in acetonitrile, unless otherwise indicated) and mild heat to allow the CsBr to fully react (see **Figure S2**). After the desired reaction time, the reaction was cooled to room temperature and transferred to a centrifuge tube using ethanol. The solutions were centrifuged at 5000 rpm for 4 minutes, after which the powder was washed once with ethanol and then dried overnight in an oven at 120 °C.

Synthesis of Cs_2TeBr_6 from TeO_2: In a 20 mL scintillation vial, 0.25 mmol (40 mg) TeO_2 was dissolved in 3 mL of hydrobromic acid and, if desired, 10 mL of an organic solvent. Complete dissolution requires stirring and heating up to ~60 °C. Upon complete dissolution of the white TeO_2 powder, 0.5 mmol CsBr (106 mg) was directly added to the solution as a solid. The reaction was then immediately removed from the hot plate, allowed to cool to room temperature, and transferred to a centrifuge tube using ethanol to aid in completely transferring any powder. The solutions were centrifuged at 5000 rpm for 4 minutes, after which the powder was washed once with ethanol and then dried overnight in an oven at 120 °C.

Powder X-ray diffraction (PXD): Laboratory PXRD was collected on a PANalytical Empyrean diffractometer. Powders were loaded onto silicon substrates and probed in Bragg-Brentano geometry using Cu Kα radiation. Synchrotron PXRD was collected via the 11-BM mail-in program at the Advanced Photon Source at Argonne National Laboratory. Powders were loaded into 1 mm Kapton capillaries and probed in transmission mode using an X-ray energy of 27 keV.

Scanning electron microscopy (SEM): SEM images were collected on the FEI Nova Nano 650 or the Thermo Scientific Apreo C LoVac SEM. Powder was dispersed on top of copper tape and imaged with an accelerating voltage of 10 kV (or 3 to 5 kV on the Apreo C) and a beam current of 0.4 nA.

UV-Vis absorption and reflectance spectroscopy: Absorption spectra of solutions and diffuse reflectance spectra of powders were acquired using the integrating sphere attachment of a Shimadzu UV3600 UV-Vis-NIR spectrometer. Solution spectra were acquired in 1 cm cuvettes. Powders were diluted in a 1:4 volume ratio with $BaSO_4$ (see **Figure S3**). Reflectance spectra were converted to pseudo-absorbance using the Kubelka-Munk transformation.

Photoluminescence spectroscopy: Steady state emission spectra were acquired through front-face excitation of powders with a 405 nm CrystaLaser laser diode. Emission was collected in a right-angle geometry and passed through a 430 nm long pass filter to an Acton SP500 spectrometer equipped with a PIXIS: 400 Si CCD camera.

To facilitate measurement of time-resolved emission, Cs_2TeBr_6 powders were encapsulated in RTV-615 silicone on a quartz coverslip and then cooled in a liquid nitrogen cryostat to 77 K. Cooling the samples significantly increased their emission intensity and lengthened their emission lifetimes. Samples were photoexcited using the frequency-doubled output of an 800 nm SpectraPhysics Tsunami Ti:Sapphire laser with the repetition rate reduced to 200 kHz – 2 MHz using a homemade acousto-optical pulse picker. Emission was detected by

an MPD avalanche photodiode, and the emission transients were analyzed by a Becker and Hickl SPC-630 time-correlated single photon counting board.

Raman spectroscopy: Raman spectra were acquired on a Horiba Jobin Yvon T6400 confocal Raman microscope equipped with a liquid nitrogen-cooled CCD array detector and an 1800 g/mm grating. Samples were pumped using the 647 nm laser line of a krypton ion gas laser sent through a 10× microscope objective.

Results/Discussion

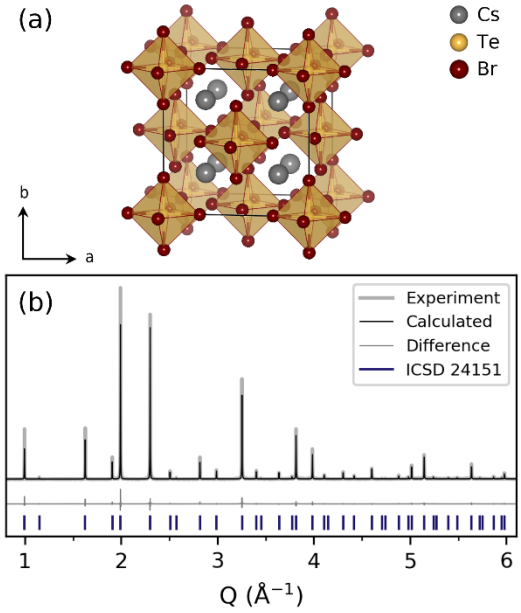

Figure 1. (a) Cs_2TeBr_6 $Fm\bar{3}m$ crystal structure. **(b)** Synchrotron powder X-ray diffraction pattern of Cs_2TeBr_6 synthesized from TeO_2 in HBr showing a calculated fit using Rietveld refinement.

Cs_2TeBr_6 powder was synthesized via two routes: the addition of solid CsBr to either the tellurium halide salt (**Figure S4a** and **Equation 1**) or the oxide (**Figure S4b** and **Equation 2**) dissolved in an organic solvent. In the latter case, concentrated hydrobromic acid (HBr) is required both as a reagent and for the dissolution of TeO_2, which is not soluble in any organic solvents; water is therefore also present as a co-solvent.

$$TeBr_4 + 2\ CsBr \rightarrow Cs_2TeBr_6 \quad (1)$$

$$TeO_2 + 4\ HBr + 2\ CsBr \rightarrow Cs_2TeBr_6 + 2\ H_2O \quad (2)$$

When $TeBr_4$ is used, the reaction time and product purity depend heavily on the solvent that is selected, with methanol requiring the shortest reaction time and always resulting in a phase-pure

product that does not contain any trace of CsBr. Synthesis proceeds readily from TeO_2 in hydrobromic acid (with or without additional organic solvent) as confirmed via laboratory PXRD (**Figure S5** and **Table S1**). The resulting product in both cases has the cubic $Fm\bar{3}m$ structure shown in **Figure 1a**, which is confirmed via synchrotron powder X-ray diffraction (PXRD) as shown in **Figure 1b**. The structure comprises spatially isolated $[TeBr_6]^{2-}$ octahedra separated by Cs^+ cations. Both $TeBr_4$ and TeO_2 already feature Te^{4+} in an octahedral coordination environment, either through direct coordination to six bromide anions ($TeBr_4$) or through coordination to five oxygen species and a sterically active lone pair (TeO_2). Notably, although Te^{4+} is in the correct coordination environment in $TeBr_4$, it is not directly accessible; the structure consists of sets of edge-sharing $[TeBr_6]^{2-}$ octahedra that together form cubic $(TeBr_4)_4$ clusters (see **Figure S4a**).

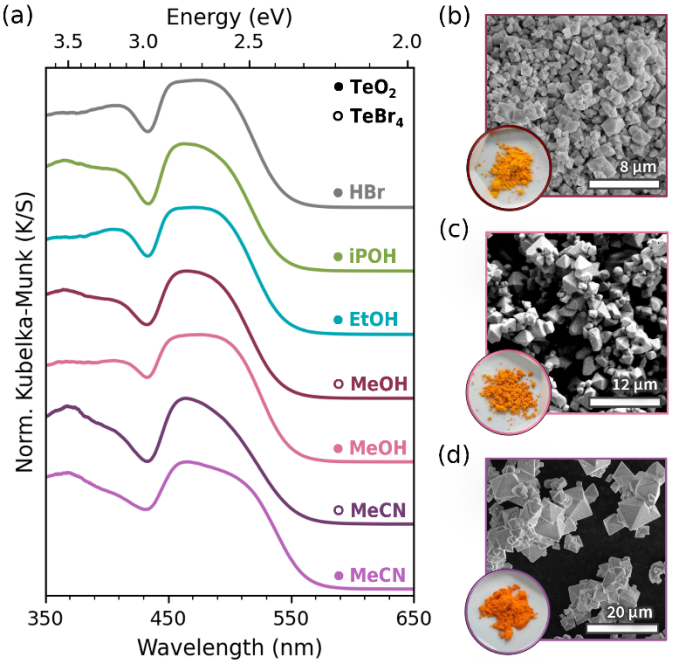

Figure 2. (a) Normalized diffuse reflectance spectra of Cs_2TeBr_6 powders synthesized from $TeBr_4$ or TeO_2 in different solvents converted to absorbance using the Kubelka-Munk transform. **(b-d)** Scanning electron microscopy (SEM) images and optical photographs of Cs_2TeBr_6 powders synthesized from **(b)** $TeBr_4$ in methanol, **(c)** TeO_2 in methanol and HBr, or **(d)** TeO_2 in acetonitrile and HBr.

The resulting powders exhibit different characteristics, such as color (varying shades of orange), consistency (chalkiness), and particle size and shape. The variations in the absorption edge were measured *via* diffuse reflectance spectroscopy in **Figure 2a** and varying particle sizes and morphologies were determined *via* scanning electron microscopy (SEM) in **Figures 2b-d** and **Figure S6.** Our absorption edge energies range from 2.12 eV to 2.24 eV, which falls in the range of collected literature values spanning from 2.06 eV to 2.29 eV (see **Table S2**). Despite differences

in absorption, all of the powders emit at the same energy (**Figure 3a**), just with differences in relative emission intensity and photoluminescence lifetime (**Figure 3b** and **Table S3**). At 77 K, the powders synthesized using alcohols or alkyl acetates have emission lifetimes ranging from 7.1 to 8.5 ns, whereas those synthesized from TeO_2 in either acetonitrile and HBr or just HBr have lifetimes of 37 and 86 ns, respectively.

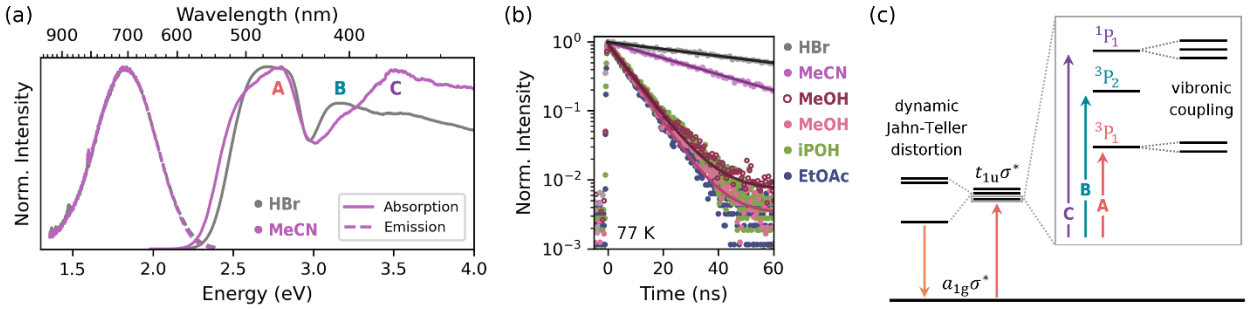

Figure 3. (a) Normalized Kubelka-Munk absorption and steady-state emission spectra of Cs_2TeBr_6 powders excited at 405 nm. Despite a difference in absorption onset, there is no difference in emission energy. **(b)** Time-resolved emission at 77 K for Cs_2TeBr_6 powders excited at 400 nm. Symbols differentiating $TeBr_4$ *vs.* TeO_2 are consistent with Figure 2. **(c)** Scheme depicting absorption and emission transitions in Cs_2TeBr_6 based on the molecular orbitals of $[TeBr_6]^{2-}$. Excitation promotes an electron from the $\boldsymbol{a_{1g}\sigma^*}$ to the triply degenerate $\boldsymbol{t_{1u}\sigma^*}$ orbital, creating either a singlet ($\mathbf{^1P_1}$) or triplet ($\mathbf{^3P_1}$ or $\mathbf{^3P_2}$) state, the energies of which are slightly different. Vibronic coupling splits the structure of the $\mathbf{^1P_1}$ and $\mathbf{^3P_1}$ states. Once in the excited state, the structure undergoes a dynamic (i.e. pseudo or second-order) Jahn-Teller distortion *via* vibronic coupling to the $\boldsymbol{e_g}$ vibration, lowering the symmetry of the $[TeBr_6]^{2-}$ sites from $\boldsymbol{O_h}$ to $\boldsymbol{D_{4h}}$.

The isolated nature of the $[TeBr_6]^{2-}$ clusters in the Cs_2TeBr_6 structure is evident in the absorption and emission spectra shown in **Figure 3a**. The absorption spectrum of Cs_2TeBr_6 is dominated primarily by the absorption of the molecular $[TeBr_6]^{2-}$ ion, in which excitation of a $5s^2$ electron into a p orbital enables the formation of either a spin-allowed singlet ($^1P_1$) or a spin-forbidden triplet excited state ($^3P_0$, $^3P_1$, or $^3P_2$).[61,62] The molecular nature of the Cs_2TeBr_6 absorption is highlighted by the fact that the same spectrum can be reproduced by doping small amounts of Te^{4+} into a matrix of a higher band gap VODP, such as A_2MCl_6 (M = Sn, Zr); at just 0.1–0.3 mol% Te^{4+}, the absorption and emission of Cs_2TeCl_6 clearly emerge from a matrix of Cs_2ZrCl_6.[5,63,64] This can also be captured from the band structure, which demonstrates that the $5s^2 \rightarrow 5s^15p^1$ transition is effectively responsible for the indirect nature of the band gap. The valence band maximum (VBM) and conduction band minimum (CBM) are primarily composed of the Te 5s and 5p orbitals, respectively, mixed with the Br 4p orbitals, leading to an indirect band gap between the W and L points (contrary to other direct band gap VODPs, where there is no involvement from the np orbital).[11,13,15]

The three transitions at 460, 405, and 370 nm (labeled A, B, and C, respectively) can thus be assigned using spin selection rules and spin-orbit coupling considerations for the $5s^2 \rightarrow 5s^15p^1$ excitation in isolated $[TeBr_6]^{2-}$ ions. Namely, since only the formation of the singlet state is completely allowed, this can be assigned to the strongest absorption peak at 370 nm (C). (Note that the transition at 370 nm is by far the strongest transition in solution; see **Figure 6b**.) For the triplet transitions, angular momentum selection rules strictly forbid the transition to $^3P_0$. However, formation of $^3P_1$ will be allowed and enhanced for systems with large spin-orbit coupling, like those containing tellurium. The second strongest transition at 460 nm can therefore be assigned to this transition (A), leaving the transition to $^3P_2$ for the weakest band at 405 nm (B).[61,62] Note that the A and C bands split into a doublet and triplet, respectively, due to coupling to a_{1g}, t_{2g}, and e_g vibrations through the dynamic Jahn-Teller effect.[61,65–67]

While the exact assignment of the transitions leading to emission in VODPs is not agreed upon, the nature of the isolated octahedra in the VODP structure is conducive to second-order (i.e. dynamic) Jahn-Teller distortions. Unlike first-order Jahn-Teller distortions, wherein the electronic state degeneracy of a structure is spontaneously lifted *via* symmetry breaking, no electronic degeneracy is required for second-order Jahn-Teller distortion to occur.[68] Instead, symmetry breaking and the adoption of a lower energy conformation occurs *via* vibronic coupling with at least two electronic states. In the case of Cs_2TeBr_6, Jahn-Teller distortion arises from coupling to the e_g vibration, leading to a symmetry reduction to D_{4h} at the metal centers and highly broadened emission.[69] **Figure 3c** summarizes these absorption and emission processes in Cs_2TeBr_6.

Particle Size Effect

The SEM images in **Figure 2b** point to particle size as a potential source of the variation in optical properties between samples. To test this hypothesis, we probed both the microscopic structure and the macroscopic particle size to determine which was the source of the variation in optical absorption and powder color. As shown in **Figure 4a**, particle size correlates with the absorption edge values determined from fitting diffuse reflectance spectra using the Tauc method. Histograms of particle size distributions obtained from measuring 90+ particles for each sample in ImageJ are shown in **Figure S6**, and example Tauc plots and fits are provided in **Figure S8** and **Table S4**. Conversely, **Figure 4b** demonstrates that the unit cell parameters determined from fitting PXRD data using the Pawley refinement method do not directly correlate with the absorption edge. Both PXRD and Raman spectroscopy also confirm that the powders are

compositionally pure, with no incorporated oxygen or solvent that would affect the electronic structure (see **Figure S7**).

It is worth emphasizing that the absorption edge shifts are not changes to the Cs_2TeBr_6 band gap. Often, experimental band gaps are determined by fitting absorption edges either directly from the absorption spectrum or by using a Tauc plot.[70,71] However, these methods do not necessarily represent the band gap (the difference in energy between the valence band maximum and conduction band minimum), as they do not account for defects or dopants that introduce sub-band gap states[72–74] or the exciton binding energy. The absorption onset determined from a diffuse reflectance spectrum using the Kubelka-Munk transformation depends on several factors, such that parameters such as particle size and shape impact the degree of scattering and modify the shape of the absorption spectrum.[75,76] While all of these factors provide a useful handle on optical properties, they do not strictly modify the band gap, and care should be taken when comparing the absorption edge observed via diffuse reflectance spectroscopy to computational values.

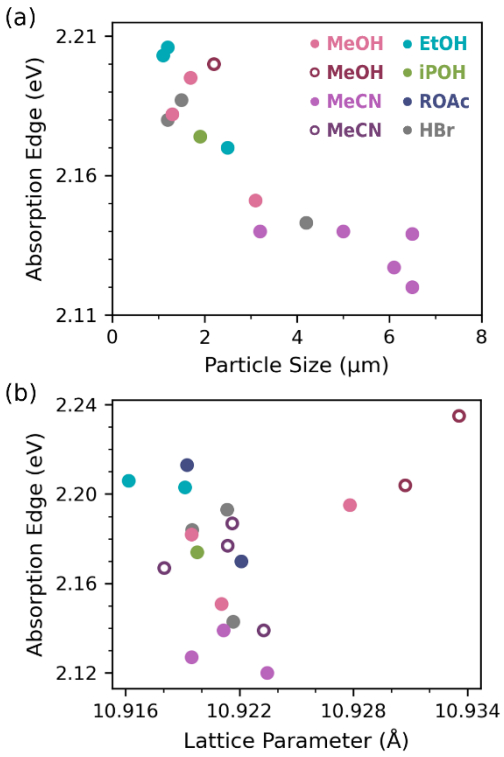

Figure 4. (a) Absorption edge as a function of particle size. Absorption edges were determined by fitting Tauc plots to indirect band gaps. Particle sizes were measured from SEM images. Symbols differentiating $TeBr_4$ *vs.* TeO_2 are consistent with Figure 2. **(b)** Absorption edges as a function of lattice parameters, which were determined by fitting PXRD patterns using Pawley refinement.

To further demonstrate the effect that particle size has on the absorption edge, we ground Cs_2TeBr_6 powder from the synthesis that led to the largest particle sizes (synthesis of Cs_2TeBr_6 from TeO_2 in HBr and MeCN) to systematically decrease particle size as a function of grinding time. Confirmation of decreased particle size was tracked via SEM and PXRD, which revealed broadened Bragg reflections following grinding (see **Figure S9**). As shown in **Figure 5a**, after just 5 minutes of grinding, the absorption edge shifts by 20 nm. (See **Table S5** for absorption edge values.) Furthermore, the molecular absorption feature of $[TeBr_6]^{2-}$ at 460 nm becomes more prominent, without the significant broadening shown by the powders in **Figure 2a**. As shown in **Figure 5b**, grinding also increases the overall absorbance of the material, such that after 20 min of grinding there is a six-fold increase in absorption at 2.7 eV and ten-fold increase at 4.0 eV. This observation is consistent with previous reports of size-dependent absorption in $KMnO_4$ particles, where reduction in particle size leads to not only an increase in scattering (*i.e.* color change) but also a reduction in specular reflection.[76] Since both ordinary and Fresnel diffuse reflection are detected during the acquisition of a "diffuse" reflection spectrum, the latter of which is actually a type of specular reflection that only appears diffuse, reduction of specular reflection leads to a lower diffuse reflectance value and therefore a higher apparent Kubelka-Munk absorbance. The fact that grinding—and more specifically, the particle size and shape—can change the absorption onset in such a dramatic way means that the peak energy, rather than the absorption onset, may be more helpful in interpreting photophysical phenomena such as the Stokes shift. For example, one recent paper reported a 90 nm shift in the absorption onset when the cesium cation in Cs_2TeBr_6 was replaced with a crown ether complex.[77] Here, we observe a 40 nm shift in the onset without any change in composition, simply by grinding the particles. Re-interpreting their data in the context of the A band peak position, which does not change position upon grinding, gives only a 13 nm shift and helps remove any influence from scattering.

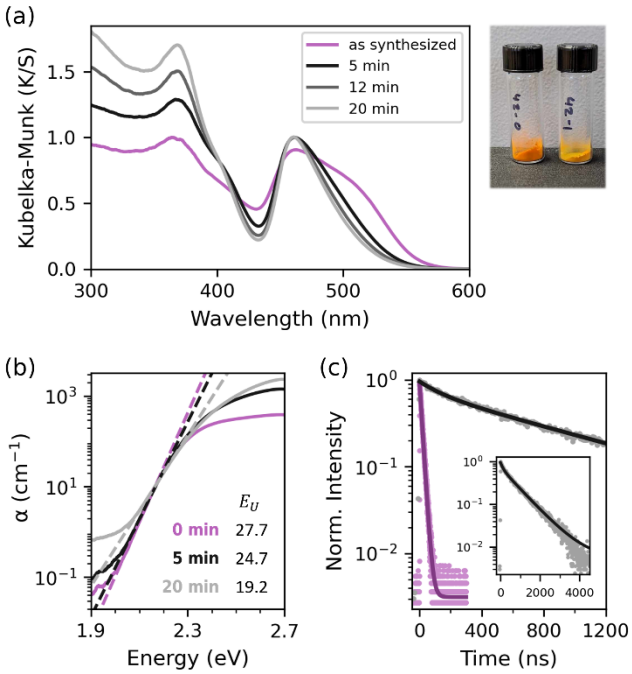

Figure 5. Effect of particle grinding on optical properties. **(a)** Normalized Kubelka-Munk absorbance spectra of Cs_2TeBr_6 powders as synthesized and after grinding for 5, 12, and 20 minutes. The photograph shows the stark color change before and after grinding for just 5 minutes. **(b)** Absorption coefficient of Cs_2TeBr_6 before and after grinding. Dashed lines indicate fits to the slope at the absorption onset on the displayed logarithmic scale to obtain values for the Urbach energy, $\boldsymbol{E_U}$, which are shown on the graph in units of eV^{-1}. **(c)** Time-resolved emission of as synthesized and ground particles. Inset shows the full long-lived decay of the ground particles.

Changes to the absorption edge upon grinding have previously been related to the "Urbach tail," *i.e.* the presence of defects within the band gap that contribute to absorption.[78] The amount of disorder can be quantified by fitting the absorption onset to the Urbach energy, E_U:

$$E_U = \left[\frac{d(\ln \alpha)}{dE}\right]^{-1}$$

In the absence of disorder, a semiconductor would exhibit a vertical absorption onset with $E_U = 0$. In practice, the combination of static and dynamic disorder gives rise to sub-band gap absorption and a positive slope. As shown in **Figure 5b**, grinding decreases the slope, reducing the Urbach energy from $E_U = 27.7$ eV^{-1} for as-synthesized particles to $E_U = 19.2$ eV^{-1} for particles ground for 20 min. Grinding therefore reduces the static disorder, for example by eliminating grain boundaries or relieving strain within individual particles through annealing. This reduction in defects and disorder also manifests in an increased photoluminescence lifetime. As shown in **Figure 5c**, upon grinding the emission lifetime at 77 K increases from 15.4 ns (monoexponential

decay) to 874 ns and 136 ns (biexponential decay with 75% and 25% amplitudes). We also calculate lower Urbach energies for the MeCN and HBr samples in **Figure 3c** that show longer photoluminescence lifetimes compared to the alcohol and alkyl acetate-based Cs_2TeBr_6 powders, again consistent with the idea that lower defect densities enable longer photoluminescence lifetimes.

Reaction Mechanism: Metal Oxide *vs* Halide

To understand the source of these synthetic variations, we investigated the differences in reaction mechanism for $TeBr_4$ *vs.* TeO_2 in the varying solvents. $TeBr_4$ is soluble in many organic solvents, exhibiting only minimal solubility in non-polar solvents such as toluene and chloroform but good solubility in methyl and ethyl acetate, dimethylformamide (DMF), dimethyl sulfoxide (DMSO), acetonitrile, and alcohols. Although the alkyl acetates are of a similar polarity as chloroform, they are more strongly coordinating and allow for the possibility of coordination in a bidentate fashion, which may drive solubility. Given previous reports on the synthesis of Cs_2TeBr_6 from $TeBr_4$ in methanol, we chose to compare the synthesis of Cs_2TeBr_6 from $TeBr_4$ in three different solvents of varying polarity and coordination strength (i.e. Lewis basicity): methyl acetate (MeOAc), acetonitrile (MeCN), and methanol (MeOH). The reaction proceeded most quickly and produced the highest, nearly stoichiometric yield in MeOH, followed by MeCN (see **Table S6** for reaction yields). While there was some reactivity in MeOAc, the reaction was very slow and did not proceed to completion. This was confirmed by PXRD (**Figure S2**), which shows complete conversion in the case of MeOH and MeCN after 1 and 2 hours, respectively, but incomplete conversion with remaining CsBr after 6 hours of reaction in MeOAc. On the other hand, synthesis from TeO_2 is essentially only dependent upon the addition of HBr. Use of an organic solvent does not seem to affect its completion, except in the minor variation in the amount of time it takes to fully dissolve the TeO_2 at the beginning of the reaction. Following the addition of CsBr, all of the reactions immediately proceed to completion with nearly quantitative yield.

A mechanism for these observations can be developed through analysis of the UV-Vis absorption spectra of $TeBr_4$ in each of the three solvents (**Figure 6a**) compared to TeO_2 (**Figure 6b**). When $TeBr_4$ is dissolved in MeOAc, it forms an orange solution that features only one identifiable absorption peak at ~430 nm. On the other hand, $TeBr_4$ dissolved in MeOH is yellow with only a weak absorption feature at ~430 nm and a more prominent absorption feature at ~350 nm. Interestingly, $TeBr_4$ dissolved in MeCN captures both the absorption features at 350 nm and 440 nm (and therefore is orange). The feasibility of the reaction in MeCN and MeOH and not MeOAc suggests that this feature at 350 nm is related to the reactivity of $TeBr_4$. Specifically, prior

literature on the chemistry and reactivity of the tellurium tetrahalides identify polar solvents such as methanol, ethanol, diethyl ether, dioxane, and potentially acetonitrile as leading to the dissociation of the cubic $(TeX_4)_4$ clusters structures into ionic $[TeX_3]^+X^-$ or $[L_2TeX_3]^+X^-$ complexes (X = Cl, Br; L is a solvent molecule).[79–81] Acetonitrile is especially distinguished as leading to only partial ionization of TeX_4.[82] Our observed reaction rate trend according to MeOH > MeCN > MeOAc is therefore consistent with the conclusion that a polar solvent is necessary to enable the dissociation of $(TeBr_4)_4$ clusters into intermediate $[L_2TeX_3]^+X^-$ complexes and ensuing Cs_2TeBr_6 production. **Figure 6c** summarizes this process, showing our interpretation of the reaction proceeding through an $[L_2TeX_3]^+X^-$ intermediate given the coordinating nature of both methanol and acetonitrile.

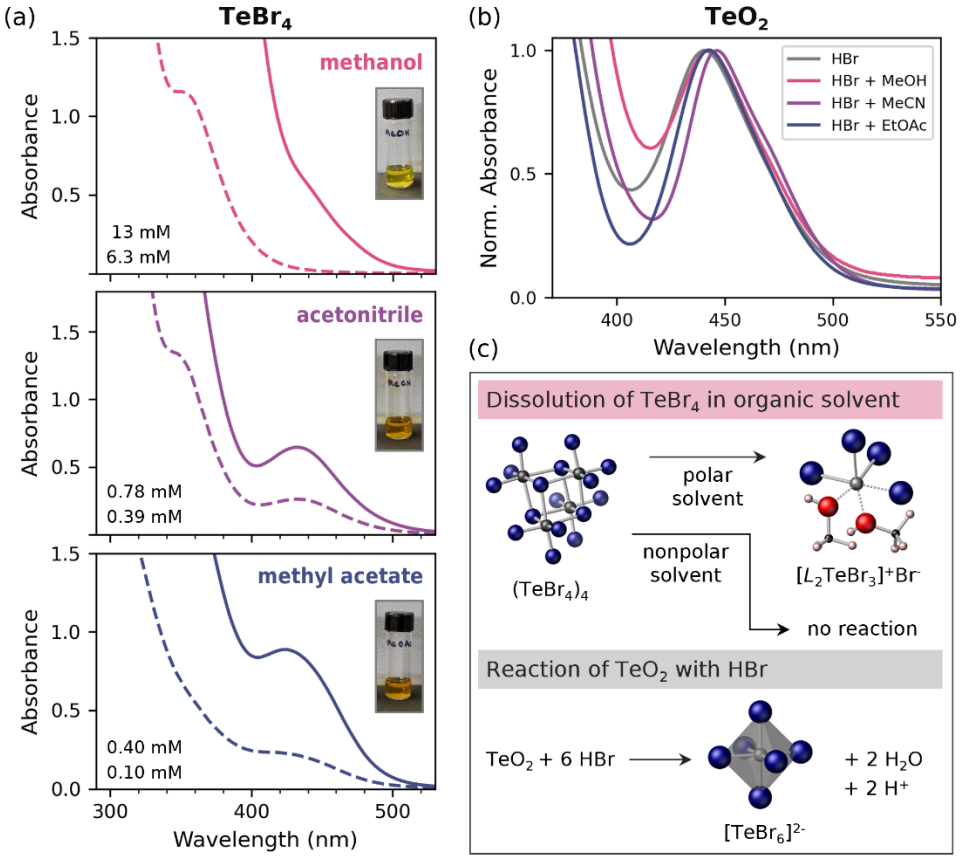

Figure 6. (a) UV-Vis absorption spectra of $TeBr_4$ in methanol, acetonitrile, and methyl acetate at the indicated concentrations. **(b)** UV-Vis absorption spectra of TeO_2 in HBr or methanol, acetonitrile, and ethyl acetate mixed with HBr. **(c)** Scheme illustrating the mechanism for dissolution of $TeBr_4$ and TeO_2 in solution. In polar solvents, $(TeBr_4)_4$ dissolves, forming $[L_2TeBr_3]^+Br^-$. Nonpolar solvents are unable to stabilize Br^-, leaving the $(TeBr_4)_4$ clusters intact. Similarly, TeO_2 is not soluble in organic solvents and requires HBr to "dissolve" and form $[TeBr_6]^{2-}$ clusters.

The synthesis of Cs_2TeBr_6 from TeO_2 proceeds without any significant variations in reaction rate or yield for all of the organic solvents surveyed (methanol, ethanol, isopropanol, methyl acetate, ethyl acetate, and acetonitrile). When TeO_2 is dissolved in these solvents with the aid of HBr, the result is the production of $[TeBr_6]^{2-}$ clusters. As such, the UV-Vis absorption spectrum does not vary aside from slight changes in the absorption wavelength. In addition to potential solvent coordination effects, these solvents alter the solution pH (**Figure S10**) and affect how quickly TeO_2 dissolves, with TeO_2 dissolving the most quickly in concentrated HBr followed by HBr diluted with MeCN, MeOAc, or MeOH (**Figure S11**). In each case, heating the solution to ~60 °C aids in dissolution. Dissolution progress (more specifically, conversion to $[TeBr_6]^{2-}$) can be monitored by the solution color change to orange, which arises from the absorption of the $[TeBr_6]^{2-}$ ion (**Figure 6b**).

Reaction Mechanism: Solvent

Given that the reaction of TeO_2 with CsBr can proceed without the addition of any organic solvent and requires HBr in all cases, one might ask what the advantage is of using organic solvent at all. In all cases, we observe nearly instantaneous and complete conversion of the reagents into Cs_2TeBr_6 upon the addition of CsBr, with solution synthesis requiring lower temperatures and shorter reaction times than solid state or hydrothermal synthesis. Ultimately, the organic solvent enables manipulation of particle size and morphology that can be beneficial depending on the application at hand. For example, in the application of VODPs for photocatalysis,[83,84] smaller particles like those produced from the reaction in methanol would provide increased surface areas and thereby increase conversion efficiencies. On the other hand, reaction in concentrated HBr without any organic solvent results in powders with longer emission lifetimes, suggesting that synthesis in HBr may be preferred for light-emitting applications.

The solvent clearly dictates a number of properties within the synthesis, namely (1) the resulting particle size and shape (morphology) and its effect on the absorption onset and (2) the intrinsic disorder and its effect on charge carrier recombination. With regards to the former, we note that the absorption onset is not dictated by either solvent polarity or dielectric constant, as this would lead to a clear delineation between those reactions done in only organic solvent (with $TeBr_4$), organic solvent with HBr (with TeO_2), or just HBr (with TeO_2). Water both is the most polar solvent used here (in the form of aqueous HBr) and has a dielectric constant that far surpasses those of the organic solvents (see **Table S7**). However, the trend in absorption onset is more consistent with the solvent donor number (see **Table S8**). The Gutmann donor number provides an estimate of the Lewis basicity of a molecule and is defined as the reaction enthalpy

for adduct/complex formation between the molecule (a Lewis base) and $SbCl_5$.[85] Solvents with high donor numbers should likewise coordinate more readily with Te^{4+}, thereby preventing the growth of large Cs_2TeBr_6 particles.[41] In the reactions performed in mixtures of HBr and organic solvent, aqueous HBr essentially dilutes the effect of the organic solvent, weakening the interaction between the solvent and the tellurium complex. The low donor number of MeCN (14.1) explains why compounds synthesized in MeCN have the lowest absorption onset, with Cs_2TeBr_6 made from TeO_2 in MeCN and HBr yielding the lowest absorption onset at 2.13 eV, since its low donor number enables the growth of large, single domain particles. As shown in **Table S8**, the absorption onset increases with the donor number; the only exception is for the particles that are synthesized in HBr only. It is possible that there is another confounding effect, like reaction time, that contributes to the final particle size and that was not controlled for in this study.

The interaction between the solvent and the tellurium complex also explains the trend in emission lifetimes, where Cs_2TeBr_6 particles made from TeO_2 in only HBr exhibit significantly longer emission decay lifetimes (86 ns) compared to those made from TeO_2 in MeCN and HBr (37 ns) or any other conditions (7.2 to 8.5 ns). It is possible that, in addition to leading to smaller particle sizes and higher absorption onset energies, solvent coordination induces strain, grain boundaries, and/or defect formation within individual particles that contributes to shortened emission lifetimes. In this case, HBr could be viewed as a relatively innocuous or even beneficial species during synthesis, as availability of Br^- ions would prevent the formation of Br^- vacancies. More importantly, it avoids the use of a more strongly coordinating solvent (such as an alcohol), where displacement of a bromide ion in the $[TeBr_6]^{2-}$ cluster with a solvent molecule would be both entropically and enthalpically favorable and could lead to the aforementioned issues, even if the solvent molecule does not remain incorporated in the crystal structure following synthesis completion.

Conclusion

In conclusion, we have synthesized Cs_2TeBr_6 from metal halide and metal oxide precursors in a number of different organic solvents. While most synthetic conditions yield powders that are phase-pure as confirmed *via* structural characterization techniques like powder X-ray diffraction, optical characterization reveals several differences stemming from solvent-directed effects. The choice of metal precursor and solvent dictate the resulting particle size and defect density, which

manifest as differences in the absorption edge and emission lifetime. These variations can be used to explain the discrepancy in the literature in reported experimental band gaps for VODPs, as the use of the absorption edge to determine the material band gap neglects contributions from sub-band gap states, defects, and the exciton binding energy and is easily manipulated by changing the scattering properties of the sample. As a demonstration of this effect, we show that grinding particles shifts the absorption edge by 40 nm, despite no change to the electronic structure. Our results highlight how synthetic methods can be used as a handle on optical and electronic properties in this emerging class of inorganic materials, and how attention should be paid to sample preparation when comparing photophysical properties among compositions.

Acknowledgements

This work was supported by the U.S. Department of Energy, Office of Science, Office of Basic Energy Sciences under Award DE-SC0024422. The research reported here made use of the shared facilities of the Materials Research Science and Engineering Center (MRSEC) (NSF DMR–2308708) and the Optical Characterization Facility (DoD ARO DURIP 66886LSRIP; DoD ONR DURIP N00014-19-1-2527) at UC Santa Barbara. The UC Santa Barbara MRSEC is a member of the Materials Research Facilities Network (www.mrfn.org). The authors acknowledge the use of the Quantum Structures Facility within the California NanoSystems Institute, supported by the University of California, Santa Barbara and the University of California, Office of the President. Use of the Advanced Photon Source at Argonne National Laboratory was supported by the U. S. Department of Energy, Office of Science, Office of Basic Energy Sciences, under Contract No. DE-AC02-06CH11357.

Supporting Information Description

Supporting Information Available: Additional methods, powder X-ray diffraction, scanning electron microscope images and particle size analysis, Raman spectra, emission lifetimes, absorption edge fits, Tauc plots, and solvent properties. This material is available free of charge *via* the Internet at http://pubs.acs.org

AUTHOR INFORMATION

Corresponding Author

* seshadri@mrl.ucsb.edu ; mchabinyc@engineering.ucsb.edu

Author Contributions

The manuscript was written through contributions of all authors. A.B. synthesized the materials with assistance from G.T.K. and E.E.M and characterized them. O.K. acquired scanning electron microscopy images and solution UV-Vis absorption spectra. A.A.M. and T.A.S. assisted with optical characterization. A.B. analyzed the data. A.B., M.C., and R.S. designed the project scope. All authors have given approval to the final version of the manuscript.

Funding Sources

DE-SC0024422, DE-AC02-06CH11357, NSF DMR–2308708, DoD ARO DURIP 66886LSRIP, DoD ONR DURIP N00014-19-1-2527

References

(1) Zhao, X.-G.; Yang, D.; Ren, J.-C.; Sun, Y.; Xiao, Z.; Zhang, L. Rational Design of Halide Double Perovskites for Optoelectronic Applications. *Joule* **2018**, *2* (9), 1662–1673. https://doi.org/10.1016/j.joule.2018.06.017.

(2) Smith, M. D.; Connor, B. A.; Karunadasa, H. I. Tuning the Luminescence of Layered Halide Perovskites. *Chem. Rev.* **2019**, *119* (5), 3104–3139. https://doi.org/10.1021/acs.chemrev.8b00477.

(3) Zhu, C.; Jin, J.; Wang, Z.; Xu, Z.; Folgueras, M. C.; Jiang, Y.; Uzundal, C. B.; Le, H. K. D.; Wang, F.; Zheng, X.; Yang, P. Supramolecular Assembly of Blue and Green Halide Perovskites with Near-Unity Photoluminescence. *Science* **2024**, *383* (6678), 86–93. https://doi.org/10.1126/science.adi4196.

(4) Liu, R.; Zhang, W.; Wen, T.; Wen, X.; Ding, C.; Li, Z.; Yan, W. Excitation-Dependent Tunable White Light of ns^2 Ions Doped Rb_2SnCl_6 Vacancy Ordered Double Perovskite. *J. Phys. Chem. Lett.* **2022**, *13* (48), 11143–11152. https://doi.org/10.1021/acs.jpclett.2c03057.

(5) Sun, J.; Zheng, W.; Huang, P.; Zhang, M.; Zhang, W.; Deng, Z.; Yu, S.; Jin, M.; Chen, X. Efficient Near-Infrared Luminescence in Lanthanide-Doped Vacancy-Ordered Double Perovskite Cs_2ZrCl_6 Phosphors via Te^{4+} Sensitization. *Angew. Chem. Int. Ed.* **2022**, *61* (26), e202201993. https://doi.org/10.1002/anie.202201993.

(6) Cao, M.; Li, Z.; Zhao, X.; Gong, X. Achieving Ultrahigh Efficiency Vacancy-Ordered Double Perovskite Microcrystals via Ionic Liquids. *Small* **2022**, *18* (44), 2204198. https://doi.org/10.1002/smll.202204198.

(7) Cai, Y.; Xie, W.; Ding, H.; Chen, Y.; Thirumal, K.; Wong, L. H.; Mathews, N.; Mhaisalkar, S. G.; Sherburne, M.; Asta, M. Computational Study of Halide Perovskite-Derived A_2BX_6 Inorganic Compounds: Chemical Trends in Electronic Structure and Structural Stability. *Chem. Mater.* **2017**, *29* (18), 7740–7749. https://doi.org/10.1021/acs.chemmater.7b02013.

(8) Lee, B.; Stoumpos, C. C.; Zhou, N.; Hao, F.; Malliakas, C.; Yeh, C.-Y.; Marks, T. J.; Kanatzidis, M. G.; Chang, R. P. H. Air-Stable Molecular Semiconducting Iodosalts for Solar Cell Applications: Cs_2SnI_6 as a Hole Conductor. *J. Am. Chem. Soc.* **2014**, *136* (43), 15379–15385. https://doi.org/10.1021/ja508464w.

(9) Blasse, G.; Dirksen, G. J.; Abriel, W. The Influence of Distortion of the Te(IV) Coordination Octahedron on Its Luminescence. *Chem. Phys. Lett.* **1987**, *136* (5), 460–464. https://doi.org/10.1016/0009-2614(87)80287-7.

(10) Sedakova, T. V.; Mirochnik, A. G.; Karasev, V. E. Structure and Luminescence Properties of Tellurium(IV) Complex Compounds. *Opt. Spectrosc.* **2011**, *110* (5), 755–761. https://doi.org/10.1134/S0030400X11030192.

(11) Cucco, B.; Katan, C.; Even, J.; Kepenekian, M.; Volonakis, G. Fine Structure of Excitons in Vacancy-Ordered Halide Double Perovskites. *ACS Mater. Lett.* **2022**, *5*, 52–59. https://doi.org/10.1021/acsmaterialslett.2c01010.

(12) Zhang, F.; Gao, W.; Cruz, G. J.; Sun, Y.; Zhang, P.; Zhao, J. Giant Excitonic Effects in Vacancy-Ordered Double Perovskites. *Phys. Rev. B* **2023**, *107* (23), 235119. https://doi.org/10.1103/PhysRevB.107.235119.

(13) Maughan, A. E.; Ganose, A. M.; Scanlon, D. O.; Neilson, J. R. Perspectives and Design Principles of Vacancy-Ordered Double Perovskite Halide Semiconductors. *Chem. Mater.* **2019**, *31* (4), 1184–1195. https://doi.org/10.1021/acs.chemmater.8b05036.

(14) Folgueras, M. C.; Jin, J.; Gao, M.; Quan, L. N.; Steele, J. A.; Srivastava, S.; Ross, M. B.; Zhang, R.; Seeler, F.; Schierle-Arndt, K.; Asta, M.; Yang, P. Lattice Dynamics and Optoelectronic Properties of Vacancy-Ordered Double Perovskite Cs_2TeX_6 (X = Cl^-, Br^-, I^-) Single Crystals. *J. Phys. Chem. C* **2021**, *125* (45), 25126–25139. https://doi.org/10.1021/acs.jpcc.1c08332.

(15) Pal, B.; Kale, A. J.; Sharma, M.; Bhamu, K. C.; Kang, S. G.; Singh, V. K.; Dixit, A. Inorganic Cs_2TeX_6 (X = Cl, Br, I) Lead-Free Vacancy-Ordered Double-Perovskite Absorber-Based Single-Junction Solar Cells with a Higher Efficiency of ~24%: Theoretical Insights. *Energy Fuels* **2024**, acs.energyfuels.3c03030. https://doi.org/10.1021/acs.energyfuels.3c03030.

(16) Xu, Z.; Jiang, X.; Cai, H.; Chen, K.; Yao, X.; Feng, Y. Toward a General Understanding of Exciton Self-Trapping in Metal Halide Perovskites. *J. Phys. Chem. Lett.* **2021**, *12* (43), 10472–10478. https://doi.org/10.1021/acs.jpclett.1c02291.

(17) Tan, J.; Li, D.; Zhu, J.; Han, N.; Gong, Y.; Zhang, Y. Self-Trapped Excitons in Soft Semiconductors. *Nanoscale* **2022**, *14* (44), 16394–16414. https://doi.org/10.1039/D2NR03935D.

(18) Williams, R. T.; Song, K. S. The Self-Trapped Exciton. *J. Phys. Chem. Solids* **1990**, *51* (7), 679–716. https://doi.org/10.1016/0022-3697(90)90144-5.

(19) Dai, Z.; Lian, C.; Lafuente-Bartolome, J.; Giustino, F. Excitonic Polarons and Self-Trapped Excitons from First-Principles Exciton-Phonon Couplings. *Phys. Rev. Lett.* **2024**, *132* (3), 036902. https://doi.org/10.1103/PhysRevLett.132.036902.

(20) Ju, M.-G.; Chen, M.; Zhou, Y.; Garces, H. F.; Dai, J.; Ma, L.; Padture, N. P.; Zeng, X. C. Earth-Abundant Nontoxic Titanium(IV)-Based Vacancy-Ordered Double Perovskite Halides with Tunable 1.0 to 1.8 eV Bandgaps for Photovoltaic Applications. *ACS Energy Lett.* **2018**, *3* (2), 297–304. https://doi.org/10.1021/acsenergylett.7b01167.

(21) Aslam, S.; Farooqi, A. S.; Rahman, M. Y. A.; Samsuri, S. A. M. Titanium-Based Vacancy-Ordered Double Halide Family in Perovskite Solar Cells. *Phys. Status Solidi A* **2022**, *219* (8), 2100671. https://doi.org/10.1002/pssa.202100671.

(22) Maughan, A. E.; Ganose, A. M.; Bordelon, M. M.; Miller, E. M.; Scanlon, D. O.; Neilson, J. R. Defect Tolerance to Intolerance in the Vacancy-Ordered Double Perovskite Semiconductors Cs_2SnI_6 and Cs_2TeI_6. *J. Am. Chem. Soc.* **2016**, *138* (27), 8453–8464. https://doi.org/10.1021/jacs.6b03207.

(23) Zhang, L.; Li, S.; Sun, H.; Fang, Y.; Wang, Y.; Wang, K.; Jiang, H.; Sui, L.; Wu, G.; Yuan, K.; Zou, B. Manipulating Lone-Pair-Driven Luminescence in 0D Tin Halides by Pressure-Tuned Stereochemical Activity from Static to Dynamic. *Angew. Chem.* **2023**, *135* (46), e202311912. https://doi.org/10.1002/ange.202311912.

(24) Jiang, X.; Tao, Y.; Gu, J.; Jin, L.; Li, C.; Zhang, W.; Fu, Y. Broadband Emission Originating from the Stereochemical Expression of $6s^2$ Lone Pairs in Two-Dimensional Lead Bromide Perovskites. *Dalton Trans.* **2023**, *52* (42), 15489–15495. https://doi.org/10.1039/D3DT01627G.

(25) Molokeev, M. S.; Su, B.; Aleksandrovsky, A. S.; Golovnev, N. N.; Plyaskin, M. E.; Xia, Z. Machine Learning Analysis and Discovery of Zero-Dimensional ns^2 Metal Halides toward Enhanced Photoluminescence Quantum Yield. *Chem. Mater.* **2022**, *34* (2), 537–546. https://doi.org/10.1021/acs.chemmater.1c02725.

(26) Stoumpos, C. C.; Frazer, L.; Clark, D. J.; Kim, Y. S.; Rhim, S. H.; Freeman, A. J.; Ketterson, J. B.; Jang, J. I.; Kanatzidis, M. G. Hybrid Germanium Iodide Perovskite Semiconductors: Active Lone Pairs, Structural Distortions, Direct and Indirect Energy Gaps, and Strong Nonlinear Optical Properties. *J. Am. Chem. Soc.* **2015**, *137* (21), 6804–6819. https://doi.org/10.1021/jacs.5b01025.

(27) Xia, M.; Jiang, X.; Lin, Z.; Li, R. "All-Three-in-One": A New Bismuth–Tellurium–Borate Bi_3TeBO_9 Exhibiting Strong Second Harmonic Generation Response. *J. Am. Chem. Soc.* **2016**, *138* (43), 14190–14193. https://doi.org/10.1021/jacs.6b08813.

(28) Yang, Y.; Guo, Y.; Zhang, B.; Wang, T.; Chen, Y.-G.; Hao, X.; Yu, X.; Zhang, X.-M. Lead Tellurite Crystals $BaPbTe_2O_6$ and $PbVTeO_5F$ with Large Nonlinear-/Linear-Optical Responses Due to Active Lone Pairs and Distorted Octahedra. *Inorg. Chem.* **2022**, *61* (3), 1538–1545. https://doi.org/10.1021/acs.inorgchem.1c03144.

(29) Jiang, F.; Wu, Z.; Lu, M.; Gao, Y.; Li, X.; Bai, X.; Ji, Y.; Zhang, Y. Broadband Emission Origin in Metal Halide Perovskites: Are Self-Trapped Excitons or Ions? *Adv. Mater.* **2023**, *35* (51), 2211088. https://doi.org/10.1002/adma.202211088.

(30) Liu, R.; Zou, K.; Zhang, G.; Feng, M.; Li, M.; Liu, J. Competition Mechanism of Self-Trapped Excitons and Te^{4+} Ions Emission in the Te^{4+} Doped Vacancy-Ordered Double Perovskite Rb_2HfCl_6 and Its Excellent Properties. *Inorg. Chem. Front.* **2024**, 10.1039.D4QI00109E. https://doi.org/10.1039/D4QI00109E.

(31) Faizan, M.; Bhamu, K. C.; Murtaza, G.; He, X.; Kulhari, N.; AL-Anazy, M. M.; Khan, S. H. Electronic and Optical Properties of Vacancy Ordered Double Perovskites A_2BX_6 (A = Rb, Cs; B = Sn, Pd, Pt; and X = Cl, Br, I): A First Principles Study. *Sci. Rep.* **2021**, *11* (1), 6965. https://doi.org/10.1038/s41598-021-86145-x.

(32) Reyes-Francis, E.; Echeverría-Arrondo, C.; Esparza, D.; López-Luke, T.; Soto-Montero, T.; Morales-Masis, M.; Turren-Cruz, S.-H.; Mora-Seró, I.; Julián-López, B. Microwave-Mediated Synthesis of Lead-Free Cesium Titanium Bromide Double Perovskite: A Sustainable Approach. *Chem. Mater.* **2024**, *36* (3), 1728–1736. https://doi.org/10.1021/acs.chemmater.3c03108.

(33) Folgueras, M. C.; Louisia, S.; Jin, J.; Gao, M.; Du, A.; Fakra, S. C.; Zhang, R.; Seeler, F.; Schierle-Arndt, K.; Yang, P. Ligand-Free Processable Perovskite Semiconductor Ink. *Nano Lett.* **2021**, *21* (20), 8856–8862. https://doi.org/10.1021/acs.nanolett.1c03308.

(34) Wheeler, H. L. Über Doppelhalogenverbindungen des Tellurs mit Kalium, Rubidium und Cäsium. *Z. Für Anorg. Chem.* **1893**, *3* (1), 428–440. https://doi.org/10.1002/zaac.18930030151.

(35) Xiao, B.; Wang, F.; Xu, M.; Liu, X.; Sun, Q.; Zhang, B.-B.; Jie, W.; Sellin, P.; Xu, Y. Melt-Grown Large-Sized Cs_2TeI_6 Crystals for X-Ray Detection. *CrystEngComm* **2020**, *22* (31), 5130–5136. https://doi.org/10.1039/D0CE00868K.

(36) Zhou, J.; Luo, J.; Rong, X.; Wei, P.; Molokeev, M. S.; Huang, Y.; Zhao, J.; Liu, Q.; Zhang, X.; Tang, J.; Xia, Z. Lead-Free Perovskite Derivative $Cs_2SnCl_{6-x}Br_x$ Single Crystals for Narrowband Photodetectors. *Adv. Opt. Mater.* **2019**, *7* (10), 1900139. https://doi.org/10.1002/adom.201900139.

(37) Zheng, K.; Chen, B.; Xie, L.; Li, X.; Lu, B.; Wang, M.; Wu, Y.; Jiang, T.; Zhang, F.; Li, X.; Wang, Y. Vacancy-Ordered Double Perovskite $Rb_2ZrCl_{6-x}Br_x$: Facile Synthesis and Insight into Efficient Instrinsic Self-Trapped Emission. *Adv. Opt. Mater.* **2022**, *10*, 2101661.

(38) Maughan, A. E.; Ganose, A. M.; Candia, A. M.; Granger, J. T.; Scanlon, D. O.; Neilson, J. R. Anharmonicity and Octahedral Tilting in Hybrid Vacancy-Ordered Double Perovskites. *Chem. Mater.* **2018**, *30* (2), 472–483. https://doi.org/10.1021/acs.chemmater.7b04516.

(39) Morgan, E. E.; Kent, G. T.; Zohar, A.; O'Dea, A.; Wu, G.; Cheetham, A. K.; Seshadri, R. Hybrid and Inorganic Vacancy-Ordered Double Perovskites A_2WCl_6. *Chem. Mater.* **2023**, *35* (17), 7032–7038. https://doi.org/10.1021/acs.chemmater.3c01300.

(40) Rahimnejad, S.; Kovalenko, A.; Forés, S. M.; Aranda, C.; Guerrero, A. Coordination Chemistry Dictates the Structural Defects in Lead Halide Perovskites. *ChemPhysChem* **2016**, *17* (18), 2795–2798. https://doi.org/10.1002/cphc.201600575.

(41) Hamill, J. C.; Schwartz, J.; Loo, Y.-L. Influence of Solvent Coordination on Hybrid Organic–Inorganic Perovskite Formation. *ACS Energy Lett.* **2018**, *3* (1), 92–97. https://doi.org/10.1021/acsenergylett.7b01057.

(42) Ray, A.; Maggioni, D.; Baranov, D.; Dang, Z.; Prato, M.; Akkerman, Q. A.; Goldoni, L.; Caneva, E.; Manna, L.; Abdelhady, A. L. Green-Emitting Powders of Zero-Dimensional Cs_4PbBr_6: Delineating the Intricacies of the Synthesis and the Origin of Photoluminescence. *Chem. Mater.* **2019**, *31* (18), 7761–7769. https://doi.org/10.1021/acs.chemmater.9b02944.

(43) Abdelsamie, M.; Cruse, K.; Tamura, N.; Ceder, G.; Sutter-Fella, C. M. Impact of Processing Conditions on the Film Formation of Lead-Free Halide Double Perovskite $Cs_2AgBiBr_6$. *J. Mater. Chem. A* **2022**, *10* (37), 19868–19880. https://doi.org/10.1039/D2TA00763K.

(44) Hadi, A.; Ryan, B. J.; Nelson, R. D.; Santra, K.; Lin, F.-Y.; Cochran, E. W.; Panthani, M. G. Improving the Stability and Monodispersity of Layered Cesium Lead Iodide Perovskite Thin Films by Tuning Crystallization Dynamics. *Chem. Mater.* **2019**, *31* (14), 4990–4998. https://doi.org/10.1021/acs.chemmater.9b00238.

(45) Dahlman, C. J.; DeCrescent, R. A.; Venkatesan, N. R.; Kennard, R. M.; Wu, G.; Everest, M. A.; Schuller, J. A.; Chabinyc, M. L. Controlling Solvate Intermediate Growth for Phase-Pure Organic Lead Iodide Ruddlesden–Popper $(C_4H_9NH_3)_2(CH_3NH_3)_{n-1}Pb_nI_{3n+1}$ Perovskite Thin Films. *Chem. Mater.* **2019**, *31* (15), 5832–5844. https://doi.org/10.1021/acs.chemmater.9b01952.

(46) Lee, B.; Krenselewski, A.; Baik, S. I.; Seidman, D. N.; Chang, R. P. H. Solution Processing of Air-Stable Molecular Semiconducting Iodosalts, $Cs_2SnI_{6-x}Br_x$, for Potential Solar Cell Applications. *Sustain. Energy Fuels* **2017**, *1* (4), 710–724. https://doi.org/10.1039/C7SE00100B.

(47) Xu, J.; Fan, Y.; Tian, W.; Ye, L.; Zhang, Y.; Tian, Y.; Han, Y.; Shi, Z. Enhancing the Optical Absorption of Chalcogenide Perovskite $BaZrS_3$ by Optimizing the Synthesis and Post-Processing Conditions. *J. Solid State Chem.* **2022**, *307*, 122872. https://doi.org/10.1016/j.jssc.2021.122872.

(48) Rezini, B.; Seddik, T.; Mouacher, R.; Vu, T. V.; Batouche, M.; Khyzhun, O. Y. Strain Effects on Electronic, Optical Properties and Carriers Mobility of Cs_2SnI_6 Vacancy-Ordered Double Perovskite:

A Promising Photovoltaic Material. *Int. J. Quantum Chem.* **2022**, *122* (21), e26977. https://doi.org/10.1002/qua.26977.

(49) Ding, J.; Lian, Z.; Li, Y.; Wang, S.; Yan, Q. The Role of Surface Defects in Photoluminescence and Decay Dynamics of High-Quality Perovskite $MAPbI_3$ Single Crystals. *J. Phys. Chem. Lett.* **2018**, *9* (15), 4221–4226. https://doi.org/10.1021/acs.jpclett.8b01898.

(50) Chen, Y.; Lei, Y.; Li, Y.; Yu, Y.; Cai, J.; Chiu, M.-H.; Rao, R.; Gu, Y.; Wang, C.; Choi, W.; Hu, H.; Wang, C.; Li, Y.; Song, J.; Zhang, J.; Qi, B.; Lin, M.; Zhang, Z.; Islam, A. E.; Maruyama, B.; Dayeh, S.; Li, L.-J.; Yang, K.; Lo, Y.-H.; Xu, S. Strain Engineering and Epitaxial Stabilization of Halide Perovskites. *Nature* **2020**, *577* (7789), 209–215. https://doi.org/10.1038/s41586-019-1868-x.

(51) Karim, M. M. S.; Ganose, A. M.; Pieters, L.; Winnie Leung, W. W.; Wade, J.; Zhang, L.; Scanlon, D. O.; Palgrave, R. G. Anion Distribution, Structural Distortion, and Symmetry-Driven Optical Band Gap Bowing in Mixed Halide Cs_2SnX_6 Vacancy Ordered Double Perovskites. *Chem. Mater.* **2019**, *31* (22), 9430–9444. https://doi.org/10.1021/acs.chemmater.9b03267.

(52) Yang, X.; Wang, Y.; Jiang, J.; Li, M.; Tang, Z.; Cai, H.; Zhang, F.; Wu, X. Composition Effects on Structure and Optical Properties in Double Perovskite Derivatives Semiconductors $Cs_2SnI_{6-x}Br_x$ (x = 0–6). *APL Mater.* **2020**, *8* (2), 021102. https://doi.org/10.1063/1.5133151.

(53) Bhui, A.; Ghosh, T.; Pal, K.; Singh Rana, K.; Kundu, K.; Soni, A.; Biswas, K. Intrinsically Low Thermal Conductivity in the n-Type Vacancy-Ordered Double Perovskite Cs_2SnI_6: Octahedral Rotation and Anharmonic Rattling. *Chem. Mater.* **2022**, *34* (7), 3301–3310. https://doi.org/10.1021/acs.chemmater.2c00084.

(54) Saparov, B.; Sun, J.-P.; Meng, W.; Xiao, Z.; Duan, H.-S.; Gunawan, O.; Shin, D.; Hill, I. G.; Yan, Y.; Mitzi, D. B. Thin-Film Deposition and Characterization of a Sn-Deficient Perovskite Derivative Cs_2SnI_6. *Chem. Mater.* **2016**, *28* (7), 2315–2322. https://doi.org/10.1021/acs.chemmater.6b00433.

(55) Ke, J. C.-R.; Lewis, D. J.; Walton, A. S.; Spencer, B. F.; O'Brien, P.; Thomas, A. G.; Flavell, W. R. Ambient-Air-Stable Inorganic Cs_2SnI_6 Double Perovskite Thin Films *via* Aerosol-Assisted Chemical Vapour Deposition. *J. Mater. Chem. A* **2018**, *6* (24), 11205–11214. https://doi.org/10.1039/C8TA03133A.

(56) López-Fraguas, E.; Masi, S.; Mora-Seró, I. Optical Characterization of Lead-Free Cs_2SnI_6 Double Perovskite Fabricated from Degraded and Reconstructed $CsSnI_3$ Films. *ACS Appl. Energy Mater.* **2019**, *2* (12), 8381–8387. https://doi.org/10.1021/acsaem.9b01827.

(57) Mokurala, K.; Kumar, A.; Jin, S. H. Metal Work Function Effects on the Performance of UV–Visible–NIR Cs_2SnI_6 Photodetectors for Flexible Broadband Application. *Phys. Status Solidi RRL – Rapid Res. Lett.* **2024**, *18* (1), 2300107. https://doi.org/10.1002/pssr.202300107.

(58) Kaltzoglou, A.; Antoniadou, M.; Kontos, A. G.; Stoumpos, C. C.; Perganti, D.; Siranidi, E.; Raptis, V.; Trohidou, K.; Psycharis, V.; Kanatzidis, M. G.; Falaras, P. Optical-Vibrational Properties of the Cs_2SnX_6 (X = Cl, Br, I) Defect Perovskites and Hole-Transport Efficiency in Dye-Sensitized Solar Cells. *J. Phys. Chem. C* **2016**, *120* (22), 11777–11785. https://doi.org/10.1021/acs.jpcc.6b02175.

(59) Rasukkannu, M.; Velauthapillai, D.; Vajeeston, P. A First-Principle Study of the Electronic, Mechanical and Optical Properties of Inorganic Perovskite Cs_2SnI_6 for Intermediate-Band Solar Cells. *Mater. Lett.* **2018**, *218*, 233–236. https://doi.org/10.1016/j.matlet.2018.02.034.

(60) Xiao, Z.; Zhou, Y.; Hosono, H.; Kamiya, T. Intrinsic Defects in a Photovoltaic Perovskite Variant Cs_2SnI_6. *Phys. Chem. Chem. Phys.* **2015**, *17* (29), 18900–18903. https://doi.org/10.1039/C5CP03102H.

(61) Stufkens, D. J. Dynamic Jahn-Teller Effect in the Excited States of $SeCl_6^{2-}$, $SeBr_6^{2-}$, $TeCl_6^{2-}$ and $TeBr_6^{2-}$: Interpretation of Electronic Absorption and Raman Spectra. *Recl. Trav. Chim. Pays-Bas* **1970**, *89* (11), 1185–1201. https://doi.org/10.1002/recl.19700891109.

(62) Couch, D. A.; Wilkins, C. J.; Rossman, G. R.; Gray, H. B. Electronic Energy Levels in Hexahalotellurate(IV) Complexes. *J. Am. Chem. Soc.* **1970**, *92* (2), 307–310. https://doi.org/10.1021/ja00705a014.

(63) Chang, T.; Wei, Q.; Zeng, R.; Cao, S.; Zhao, J.; Zou, B. Efficient Energy Transfer in Te^{4+}-Doped Cs_2ZrCl_6 Vacancy-Ordered Perovskites and Ultrahigh Moisture Stability via A-Site Rb-Alloying Strategy. *J. Phys. Chem. Lett.* **2021**, *12* (7), 1829–1837. https://doi.org/10.1021/acs.jpclett.1c00255.

(64) Zhang, W.; Zheng, W.; Li, L.; Huang, P.; Gong, Z.; Zhou, Z.; Sun, J.; Yu, Y.; Chen, X. Dual-Band-Tunable White-Light Emission from Bi^{3+}/Te^{4+} Emitters in Perovskite-Derivative Cs_2SnCl_6 Microcrystals. *Angew. Chem.* **2022**, *134* (9), e202116085. https://doi.org/10.1002/ange.202116085.

(65) Toyozawa, Y.; Inoue, M. Dynamical Jahn-Teller Effect in Alkali Halide Phosphors Containing Heavy Metal Ions. *J Phys Soc Jpn* **1966**, *21* (9), 1663–1679.

(66) Fukuda, A. Structure of the C Absorption Band of Tl^+-Type Centers in Alkali Halides Due to the Jahn-Teller Effect. *J Phys Soc Jpn* **1969**, *27* (1), 96–109.

(67) Cho, K. Optical Absorption Line Shapes Due to Transition from Orbital Singlet to Triplet States of Defect Centers with Cubic Symmetry. *J Phys Soc Jpn* **1968**, *25* (5), 1372–1387.

(68) Bersuker, I. B. Pseudo-Jahn–Teller Effect—A Two-State Paradigm in Formation, Deformation, and Transformation of Molecular Systems and Solids. *Chem. Rev.* **2013**, *113* (3), 1351–1390. https://doi.org/10.1021/cr300279n.

(69) Wernicke, R.; Kupka, H.; Ensslin, W.; Schmidtke, H.-H. Low Temperature Luminescence Spectra of the $d^{10}s^2$ Complexes $CsMX_6$ (M=Se,Te and X=Cl, Br). The Jahn-Teller Effect in the $\Gamma_4^-(^3T_{1u}$ Excited State. *Chem. Phys.* **1979**, *47*, 235–244.

(70) Tauc, J.; Grigorovici, R.; Vancu, A. Optical Properties and Electronic Structure of Amorphous Germanium. *Phys. Status Solidi B* **1966**, *15* (2), 627–637. https://doi.org/10.1002/pssb.19660150224.

(71) Dolgonos, A.; Mason, T. O.; Poeppelmeier, K. R. Direct Optical Band Gap Measurement in Polycrystalline Semiconductors: A Critical Look at the Tauc Method. *J. Solid State Chem.* **2016**, *240*, 43–48. https://doi.org/10.1016/j.jssc.2016.05.010.

(72) Pankove, J. I. *Optical Processes in Semiconductors*, 2nd ed.; Dover Publications, 2010.

(73) Berggren, K.-F.; Sernelius, B. E. Band-Gap Narrowing in Heavily Doped Many-Valley Semiconductors. *Phys. Rev. B* **1981**, *24* (4), 1971–1986. https://doi.org/10.1103/PhysRevB.24.1971.

(74) Ugur, E.; Ledinský, M.; Allen, T. G.; Holovský, J.; Vlk, A.; De Wolf, S. Life on the Urbach Edge. *J. Phys. Chem. Lett.* **2022**, *13* (33), 7702–7711. https://doi.org/10.1021/acs.jpclett.2c01812.

(75) Landi, S.; Segundo, I. R.; Freitas, E.; Vasilevskiy, M.; Carneiro, J.; Tavares, C. J. Use and Misuse of the Kubelka-Munk Function to Obtain the Band Gap Energy from Diffuse Reflectance Measurements. *Solid State Commun.* **2022**, *341*, 114573. https://doi.org/10.1016/j.ssc.2021.114573.

(76) Diffuse Reflectance Spectroscopy. In *Modern techniques in applied molecular spectroscopy*; Mirabella, F. M., Ed.; Techniques in analytical chemistry series; Wiley: New York, 1998; pp 185–219.

(77) Zhu, C.; Jin, J.; Gao, M.; Oddo, A. M.; Folgueras, M. C.; Zhang, Y.; Lin, C.-K.; Yang, P. Supramolecular Assembly of Halide Perovskite Building Blocks. *J. Am. Chem. Soc.* **2022**, *144* (27), 12450–12458. https://doi.org/10.1021/jacs.2c04357.

(78) Waring, R. K.; Hsu, W. Y. Urbach Rule Behavior in Strongly Absorbing Fine Particle Solids. *J. Appl. Phys.* **1983**, *54* (7), 4093–4096. https://doi.org/10.1063/1.332541.

(79) Buss, B.; Krebs, B. Crystal Structure of Tellurium Tetrachloride. *Inorg. Chem.* **1971**, *10* (12), 2795–2800. https://doi.org/10.1021/ic50106a035.

(80) Couch, A.; Elmes, P. S.; Fergusson, J. E.; Wilkins, C. J. Chemistry of Selenium and Tellurium Tetrahalides : Lonisation of the Chlorides and Bromides in Solution and the Constitution of Their Adducts. *J Chem Soc A* **1967**, 1813–1817.

(81) Greenwood, N. N.; Straughan, B. P.; Wilson, A. E. Behaviour of Tellurium(IV) Chloride, Bromide, and Iodide in Organic Solvents and the Structures of the Species Present. *J Chem Soc A* **1968**, 2209–2212.

(82) Katsaros, N.; George, J. W. Solution Characteristics of Selenium and Tellurium Tetrahalides. *Inorganica Chim. Acta* **1969**, *3*, 165–168. https://doi.org/10.1016/S0020-1693(00)92470-8.

(83) Shanmugam, N.; Halpati, J. S.; Chandiran, A. K. Highly Stable and Panchromatic Light Absorbing Cs_2OsX_6 (X = Cl^-, Br^-, I^-) Vacancy Ordered Perovskites as Photoanodes for Solar Water Oxidation. *Adv. Mater. Interfaces* **2022**, 2201526. https://doi.org/10.1002/admi.202201526.

(84) Jin, J.; Huang, H.; Chen, C.; Smith, P. W.; Folgueras, M. C.; Yu, S.; Zhang, Y.; Chen, P.-C.; Seeler, F.; Schaefer, B.; Lizandara-Pueyo, C.; Zhang, R.; Schierle-Arndt, K.; Yang, P. Benzyl Alcohol Photo-Oxidation Based on Molecular Electronic Transitions in Metal Halide Perovskites. *ACS Photonics* **2023**, acsphotonics.3c00042. https://doi.org/10.1021/acsphotonics.3c00042.

(85) Gutmann, V. Solvent Effects on the Reactivities of Organometallic Compounds. *Coord. Chem. Rev.* **1976**, *18*, 225–255.

TOC Graphic

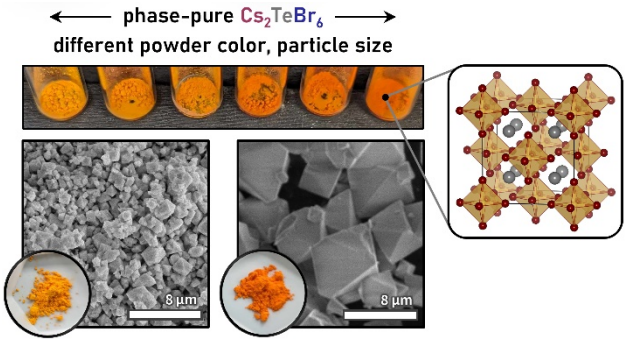
phase-pure Cs_2TeBr_6
different powder color, particle size
8 µm
8 µm

Tuning the Optical Absorption Edge of Vacancy-Ordered Double Perovskites through Metal Precursor and Solvent Selection

Alexandra Brumberg[1,2], Owen Kuklinski[1], Greggory T. Kent[1,2], Emily E. Morgan[1,2], Alexander A. Mikhailovsky[3], T. Amanda Strom[2], Michael L. Chabinyc[1,*], and Ram Seshadri[1,2,*]

[1] Department of Materials, University of California, Santa Barbara, CA 93106, United States

[2] Materials Research Laboratory, University of California, Santa Barbara, CA 93106, United States

[3] Department of Chemistry, University of California, Santa Barbara, CA 93106, United States

Contents

Methods

Method of CsBr Addition: One parameter of the synthesis that was not thoroughly explored was the method of CsBr addition. In all of the syntheses presented in the main text, CsBr was added directly to the tellurium solution as a solid, in part because HBr was not always used (for example, when working with $TeBr_4$) and CsBr is not soluble in organic solvents, but also because this is the easiest method. As **Figure S1** shows, the addition of CsBr as an acidic solution *vs.* a solid does further affect the absorption spectrum, but not as significantly as changing the organic solvent. It is plausible that the addition of CsBr as a solution prevents nucleation of Cs_2TeBr_6 on solid CsBr particles before they have had a chance to dissolve and enables a more homogenous size distribution.

We also did not investigate the effect of solution concentration on synthesis, although this likely also plays a role on particle size given that solution concentration typically dictates the nucleation and growth rates.

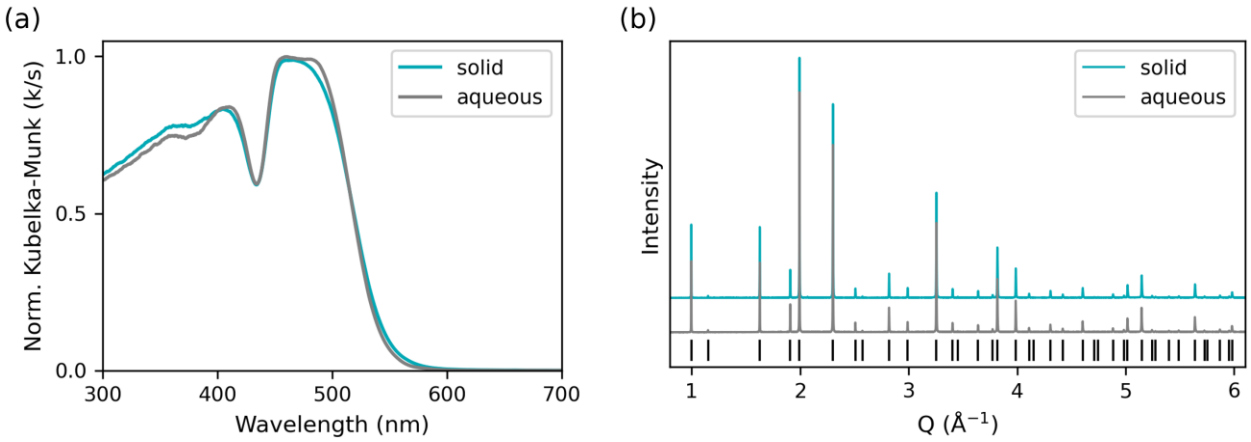

Figure S1. (a) Normalized Kubelka-Munk absorbance spectra and **(b)** synchrotron powder X-ray diffraction patterns of Cs_2TeBr_6 powders synthesized from TeO_2 and CsBr. TeO_2 was dissolved in HBr and ethanol and CsBr was added to the TeO_2 solution either directly as a solid or in the form of an aqueous acidic solution.

Reaction Time:

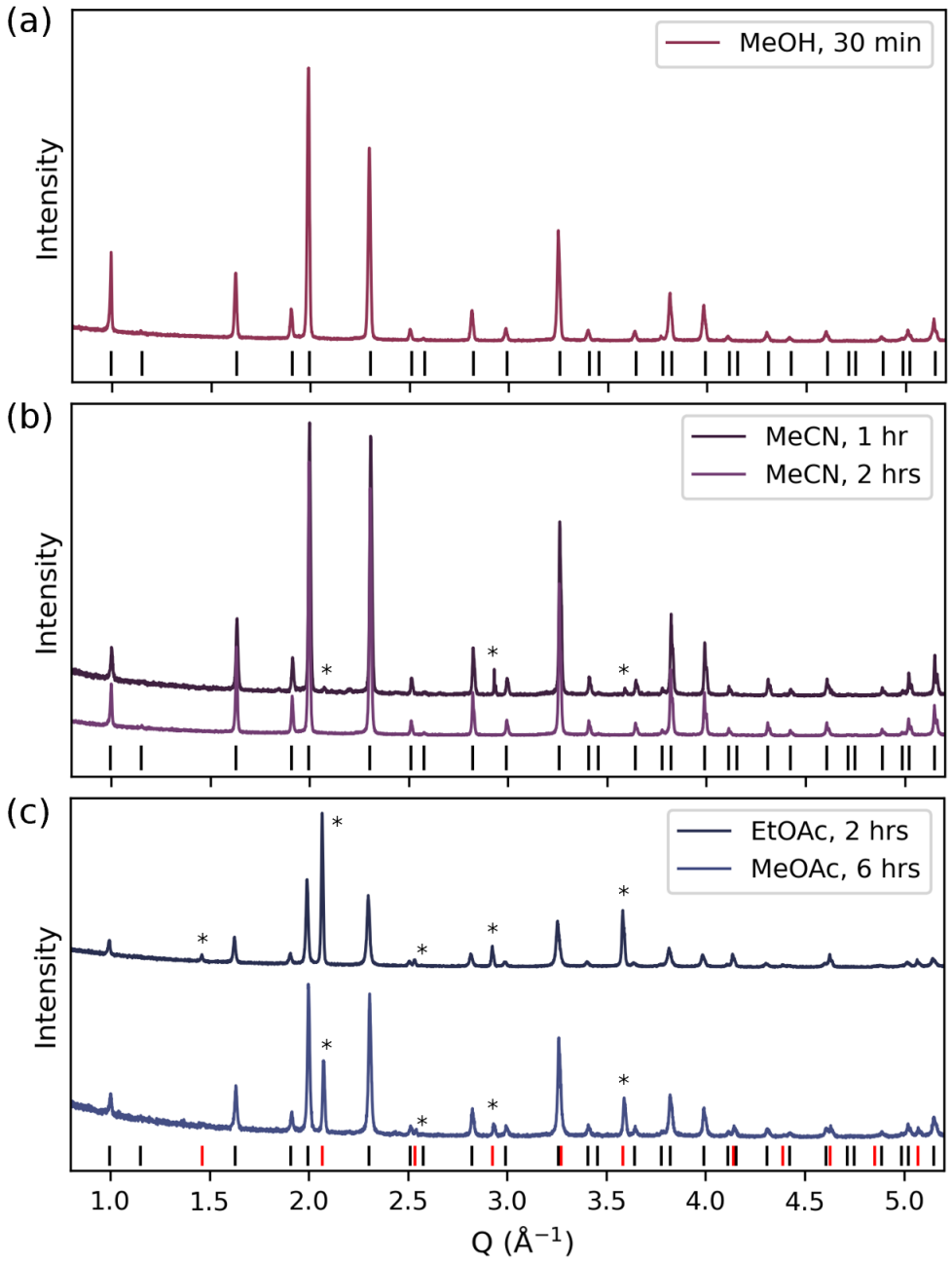

Figure S2. PXRD of Cs_2TeBr_6 following reaction of CsBr with $TeBr_4$ in **(a)** methanol, **(b)** acetonitrile, and **(c)** methyl/ethyl acetate. Asterisks indicate unreacted CsBr as established by comparision to ICSD 236387 (CsBr, red) and ICSD 24151 (Cs_2TeBr_6, black).

$BaSO_4$ Dilution: As discussed in the main text, the Kubelka-Munk transform of a diffuse reflectance spectrum depends on the scattering properties of the analyte. To properly capture the diffuse reflectance spectrum of strongly absorbing samples, it is necessary to take precautions to reduce the effects of scattering from the analyte. The first of these precautions is grinding, which is discussed in the main text. The other is sample dilution in a matrix that has minimal absorption in the region of interest (e.g. reflectance grade $BaSO_4$, a white powder).[1,2]

One aspect that is often overlooked in the literature is that the diffuse reflectance spectrum of the analyte changes as a factor of concentration in the dilutant. As such, when comparing spectra, attention must be paid that either the amount of dilutant has been corrected for (see the section on Absorption Coefficients later in the SI) or that all spectra have been collected at the same volume fraction. In this work, we chose a 1:4 ratio of analyte to dilutant for all of our spectra. As shown in **Figure S3**, further dilution continues to affect the lower energy portion of the spectrum, but the band edge remains unaffected.

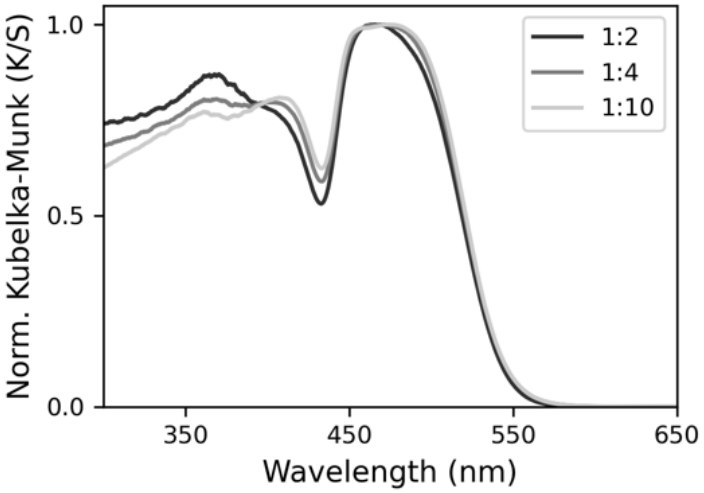

Figure S3. Normalized Kubelka-Munk reflectance spectra of Cs_2TeBr_6 powders synthesized the addition of CsBr to TeO_2 in HBr. Diffuse reflectance spectra were obtained with the specified ratios (by volume) of Cs_2TeBr_6 to $BaSO_4$.

Metal Precursor: The structures of $TeBr_4$ and TeO_2 are shown in **Figure S4**. The $(TeBr_4)_4$ cluster structure was found to play a role in how effectively various organic solvents can be used to synthesize Cs_2TeBr_6 from $TeBr_4$. Polar solvents are necessary to stabilize the ionic $[L_2TeBr_3]^+Br^-$ intermediate, without which the reaction proceeds very slowly, if at all.

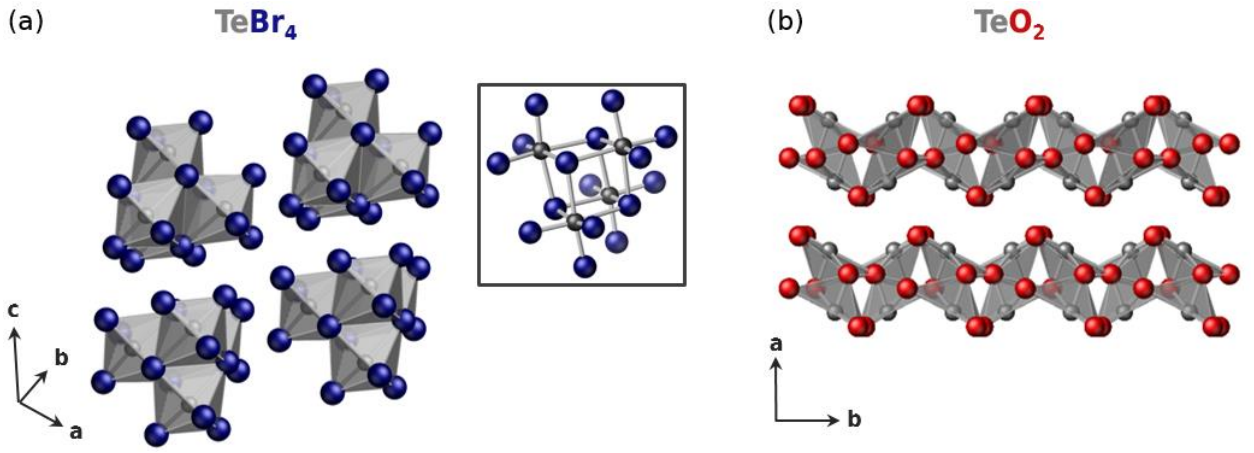

Figure S4. Crystal structures of the tellurium precursors **(a)** $TeBr_4$ and **(b)** TeO_2. Both compounds feature tellurium in a +4 oxidation state; however, $TeBr_4$ contains octahedral Te^{4+} bound as $(TeBr_4)_4$ cages, while TeO_2 contains Te^{4+} in a square pyramidal geometry that arises from coordination to five neighboring oxygens and a sterically active lone pair.

Additional Characterization

X-Ray Diffraction: As shown in **Figure S5a**, sample purity was confirmed following each synthesis using a laboratory X-ray diffractometer with Cu Kα radiation in a window of 8° to 80°. **Figure S5b** also shows that demonstrably different peak shapes were observed for the different synthetic conditions, reflecting the differences in particle shape observed in the SEM images shown in **Figure S6** and also different lattice strains. Given the variation in instrumental broadening throughout the generation of the data in this work, we did not make any further attempts to analyze the crystallite size or strain broadening present in these diffraction peaks. However, the results of the Pawley refinements presented in **Table S1** suggest that some particles do possess some amount of strain, given that a different sequence of lattice parameters (*i.e.* the ordering of largest to smallest lattice spacings) is obtained compared to what one would expected based on *d* spacings. This is true even for samples that were characterized on the same day, as is the case for the four samples shown in **Figure S5b.**

The differences in lattice parameters noted in **Table S1** are very minor, with only a 0.16% variation in a between the sample with the smallest and largest unit cell (10.916167 Å *vs* 10.93354 Å). ICSD 24151 reports a lattice parameter of a = 10.9180(20), indicating that all but one of our powders have larger lattice spacings than bulk, single crystal Cs_2TeBr_6.

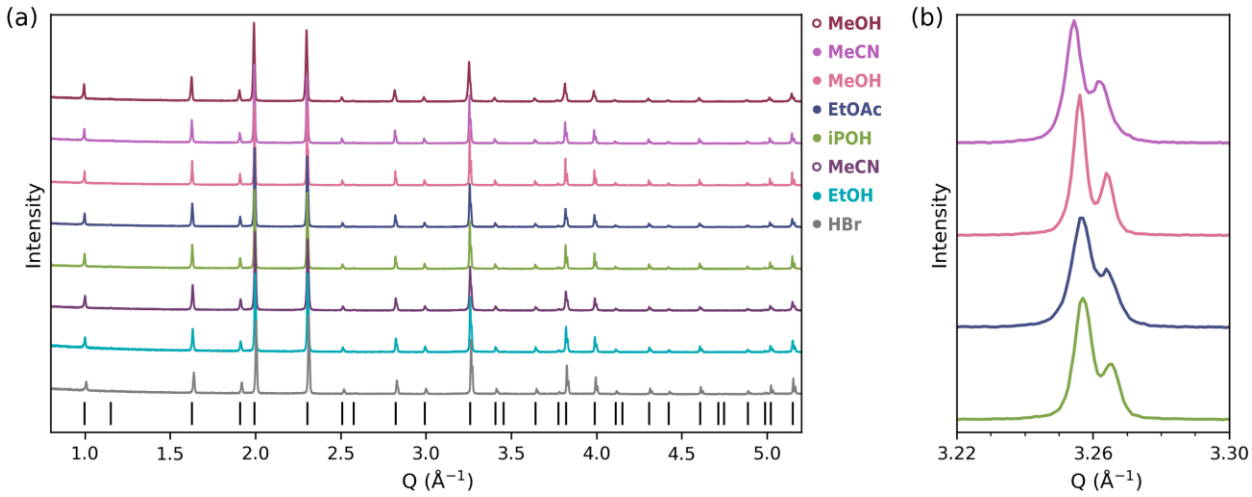

Figure S5. (a) Laboratory PXRD confirming phase purity of Cs_2TeBr_6 powders synthesized from TeO_2 and $TeBr_4$ in a variety of solvents. **(b)** Magnified diffraction pattern focusing on the (440) reflection for samples all acquired on the same day with the same collection parameters.

Table S1. Lattice parameters determined from Pawley refinements of both synchrotron and laboratory PXRD measurements on Cs_2TeBr_6 powders.

Metal Precursor	Solvent	Lattice Parameter (Å)	X-Ray Source	Notes
$TeBr_4$	**MeCN**	10.91803 ±0.00002	Synchrotron	a, b
		10.92138 ±0.00006	Lab	b
		10.92162 ±0.00004	Lab	
		10.92325 ±0.00004	Lab	
$TeBr_4$	**MeOH**	10.93071 ±0.00007	Synchrotron	
		10.93354 ±0.00003	Lab	
TeO_2	**HBr**	10.919491 ±0.000009	Synchrotron	
		10.92134 ±0.00004	Lab	
		10.9217 ±0.0002	Lab	
TeO_2	HBr + **MeCN**	10.919473 ±0.00004	Synchrotron	
		10.92115 ±0.00009	Lab	
		10.92344 ±0.00004	Lab	
TeO_2	HBr + **MeOH**	10.919473 ±0.000004	Synchrotron	
		10.92105 ±0.00003	Lab	
		10.92781 ±0.00007	Lab	
TeO_2	HBr + **EtOH**	10.916167 ±0.000007	Synchrotron	
		10.91911 ±0.00005	Lab	
TeO_2	HBr + **iPOH**	10.91976 ±0.00003	Lab	
TeO_2	HBr + **MeOAc**	10.91924 ±0.00005	Lab	b
TeO_2	HBr + **EtOAc**	10.92209 ±0.00004	Lab	

a – Reaction was stopped immediately rather than after 2 hours.

b – Some remaining CsBr.

Particle Size Analysis: Particle sizes were imaged using scanning electron microscopy and then manually measured (by approximating particles as circles and ovals) in ImageJ. Circle areas were then used to calculate particle diameters, which are shown in the histograms in **Figure S6.** This procedure generates the least accurate results for the Cs_2TeBr_6 particles synthesized from TeO_2 in HBr, which are definitively not isotropic in shape.

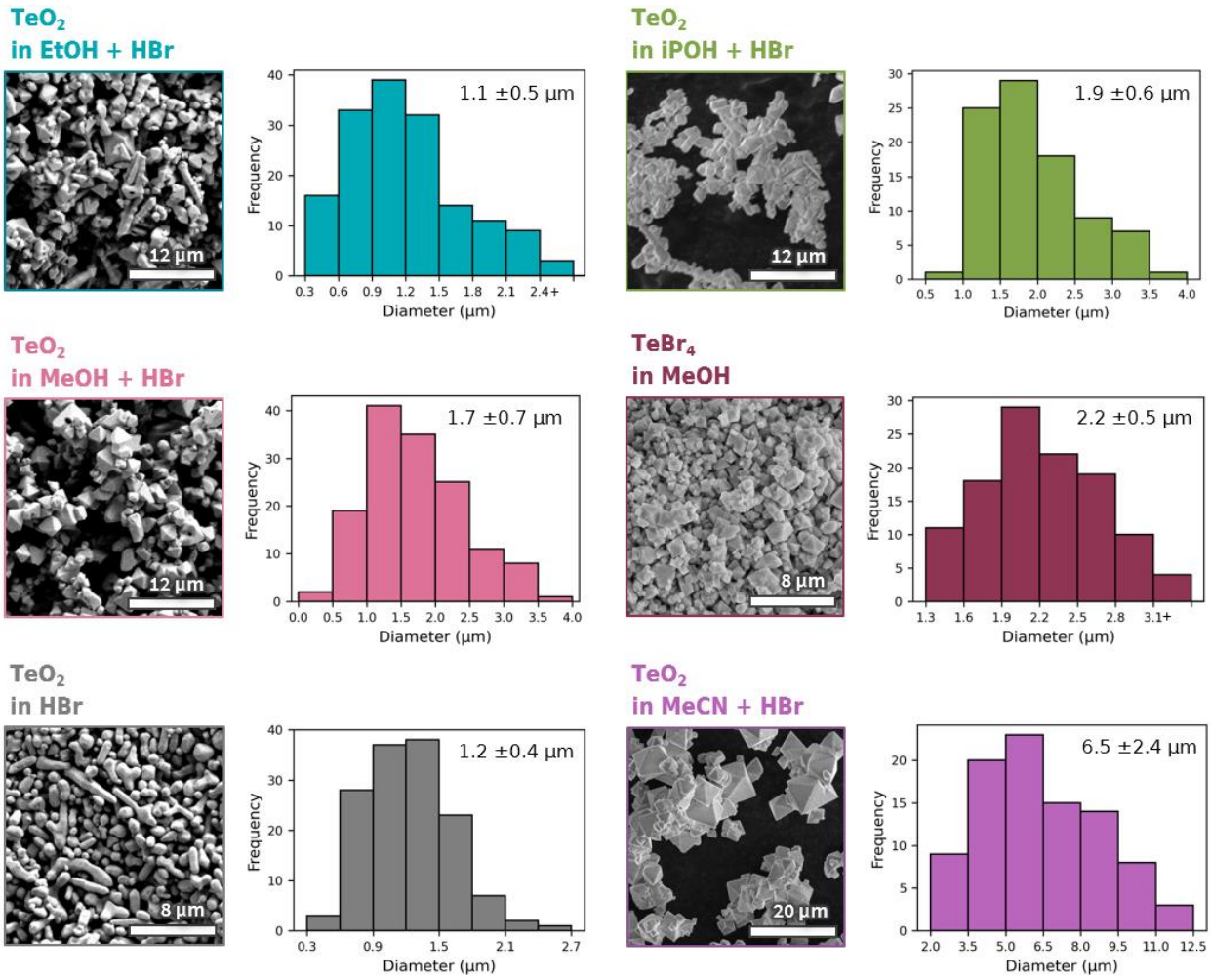

Figure S6. SEM images and sizing analyses of Cs_2TeBr_6 powders.

Raman Spectroscopy: As a further means of probing structure (*e.g.* the Te—Br bonding environment), we conducted Raman spectroscopy on Cs_2TeBr_6 powders synthesized in a variety of conditions. As shown in **Figure S7a**, we observe the E_g and A_{1g} modes that are characteristic of O_h symmetry in the $[TeBr_6]^{2-}$ clusters. The exact position of these vibrational modes varies depending on the synthetic conditions; however, it does not correlate to the absorption band edge. While vibrational frequencies provide an indication of bond strength and can be used to estimate bond lengths and therefore lattice volumes,[3,4] we did not find a correlation between our Raman spectral shifts and our PXRD lattice shifts. It is possible that, because of the isolated nature of the $[TeBr_6]^{2-}$ octahedra, changes to the Te—Br bond length are not reflected in the overall lattice parameter.

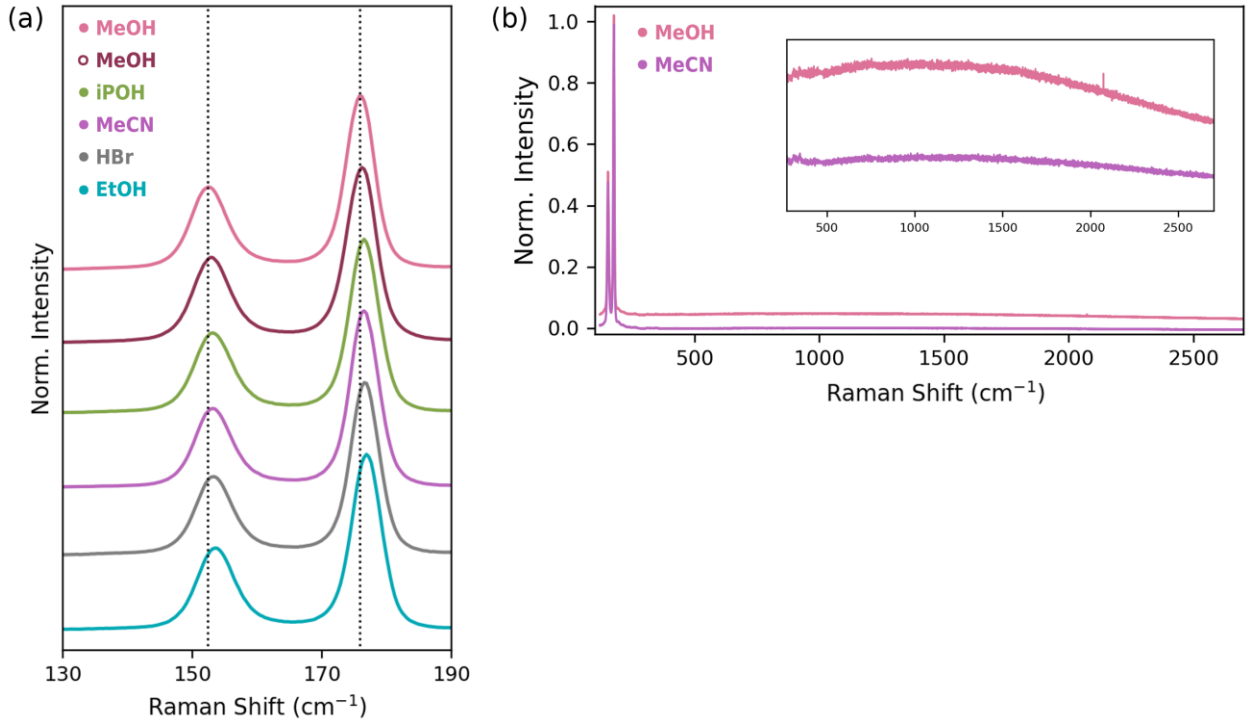

Figure S7. Raman spectra of representative Cs_2TeBr_6 powders. **(a)** Low frequency region featuring the E_g and A_{1g} vibrational modes of the $[TeBr_6]^{2-}$ octahedra. **(b)** Extended Raman spectra indicating the lack of any other spectral features, including any Te—O bonds or those corresponding to organic solvent.

We also searched the Raman spectra for any indication of oxygen or solvent that could have an effect on the crystalline or electronic structure. As shown in **Figure S7b,** we found no indication of Te—O bonding or solvent. Organic solvents would be observed around 1000 to 3000 cm^{-1}; for example, methanol is characterized by two sharp features at 1030 cm^{-1} and 1450 cm^{-1} and

two weaker features at ~1100 and 1150 cm^{-1}, while acetonitrile has two very sharp features at ~920 and 2250 cm^{-1}. No features are observed past the A_{1g} mode at ~176 cm^{-1}.

Optical Data:

Table S2. Experimentally reported absorption edges and emission wavelengths/lifetimes for Cs_2TeBr_6. Unless otherwise noted (*), absorption edge values are based on those reported in the original reference.

Reference	Synthesis Technique	Absorption Edge	Emission
Sedakova & Mirochnik[5] (2016)	Solution synthesis, heated, TeO_2 and CsBr in HBr	2.06 eV (300 K) 2.30 eV (77 K)	- 680 nm (77 K)
Li et al.[6] (2023)	Hydrothermal synthesis at 110 °C TeO_2 and CsBr in HBr	2.09 eV *,[a]	[b]
Folgueras et al.[7] JCPP (2021)	Antisolvent vapor diffusion (single crystals)	2.10 eV *	670 nm [c]
Huang et al.[8] (2022)	Hydrothermal synthesis at 180 °C $TeBr_4$ and CsBr in HCl	2.11 eV *,[a]	692 nm [d] $\tau_1 = 0.35$ ns (35%) $\tau_2 = 1.82$ ns (65%)
Peresh et al.[9] (2001)	Bridgman growth (single crystals) $TeBr_4$ and CsBr	2.12 eV	-
Folgueras et al.[10] Nano Lett. (2021)	Solution synthesis at 60 °C $TeBr_4$ in MeOH and solid CsBr	2.12 eV *	670 nm [c]
Zhu et al.[11] (2022)	Solution synthesis at RT $TeBr_4$ and CsBr in HBr	2.14 eV *	-
Jin et al.[12] (2023)	Solution synthesis at RT $TeBr_4$ in EtOH + HBr and CsBr in HBr	2.22 eV	-
Zhou et al.[13] (2024)	Hydrothermal synthesis at 180 °C $TeBr_4$ and CsBr in HCl	2.29 eV *,[a]	$\tau_{av} = 2.53$ ns [e]

* Extracted from reference absorption data using a Tauc plot.

[a] A Tauc plot was provided in the original paper; however, it was based on a direct band gap. Cs_2TeBr_6 is well established to have an indirect band gap.

[b] These authors report emission at 519 nm; however, it looks to be the edge of the 484 nm excitation they are using. Cs_2TeBr_6 has very weak emission that is difficult to detect in a fluorimeter.

[c] $\lambda_{ex} = 375$ nm [e] $\lambda_{ex} = 360$ nm

[d] $\lambda_{ex} = 365$ nm; $\lambda_{em} = 465$ nm. It is unclear how any lifetime was recorded given that the emission spectrum that was recorded for Cs_2TeBr_6 shows no emission at 465 nm.

Table S3. Emission lifetimes of Cs_2TeBr_6 powders at 77 K excited at 400 nm.

Metal Precursor	Solvent	Emission Lifetime (ns)
TeO_2	HBr + MeOH	7.16 ±0.06
TeO_2	HBr + EtOAc	7.35 ±0.04
$TeBr_4$	MeOH	8.35 ±0.06
TeO_2	HBr + iPOH	8.50 ±0.05
TeO_2	HBr + MeCN	36.8 ±0.3
TeO_2	HBr	86.2 ±0.5

Table S4. Absorption edges as determined from indirect band gap Tauc plots (see **Figure S8**). Only the conditions for which we saw relatively consistent results (±0.01 eV) are reported here. For other samples reported in this work, we either did not run enough trials to accurately report the absorption onset or there was a significant variation in the observed absorption onsets between different synthesis trials.

Metal Precursor	Solvent	Absorption Edge (eV)
TeO_2	HBr + MeCN	2.14
$TeBr_4$	MeCN	2.17
TeO_2	HBr + MeOH	2.18
TeO_2	HBr	2.19
TeO_2	HBr + EtOH	2.20
$TeBr_4$	MeOH	2.20

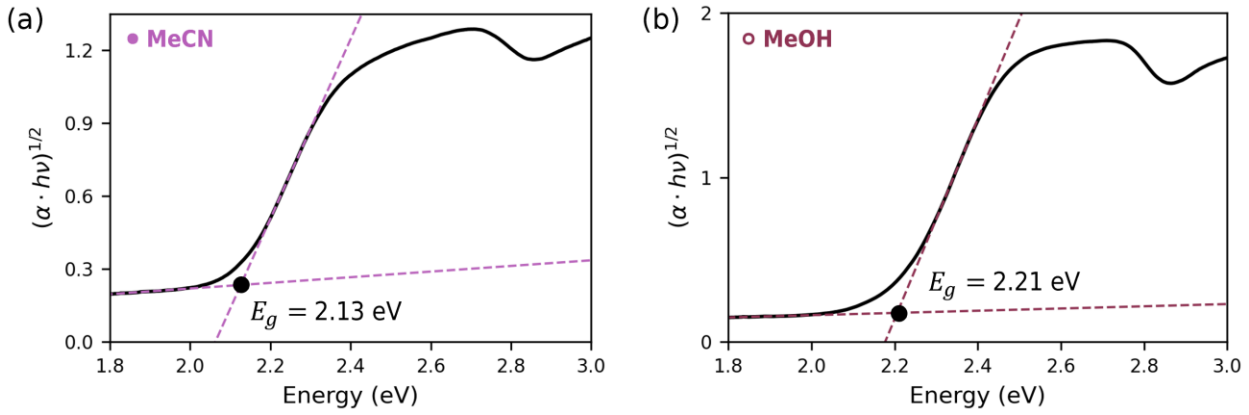

Figure S8. Examples of Tauc plots used to determine the band edge of the indirect band gap ($\gamma = 2$) semiconductor Cs_2TeBr_6 synthesized from **(a)** TeO_2 in HBr and MeCN or **(b)** $TeBr_4$ in MeOH.

Table S5. Band edges before and after grinding powders of Cs_2TeBr_6 synthesized from TeO_2 in HBr and MeCN.

Grinding Time	Band Edge (eV)
0 min (as synthesized)	2.14
5 min	2.18
12 min	2.20
20 min	2.23

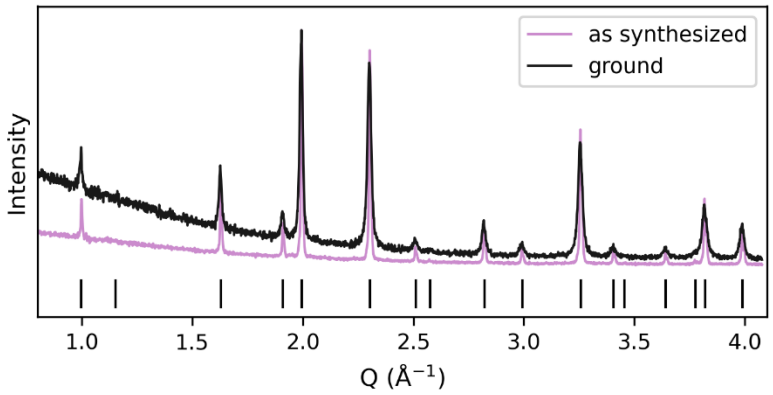

Figure S9. Powder XRD of Cs_2TeBr_6 powders as synthesized from TeO_2 in HBr and MeCN and after grinding for 5 minutes.

Absorption Coefficients: Absorption coefficients as a function of energy were determined from diffuse reflectance spectra of Cs_2TeBr_6 powders diluted in a $BaSO_4$ matrix in a 1:4 ratio. The Kubelka-Munk transform was applied to obtain $F(R_\infty)$:

$$F(R_\infty) = \frac{K}{S} = \frac{(1-R_\infty)^2}{2R_\infty}$$

where K and S are absorption and scattering coefficients, respectively. The absorption coefficient K was then isolated by multiplying by the known scattering S of the $BaSO_4$ standard; recall that dilution with a white standard such as $BaSO_4$ helps ensure that scattering is dominated by the standard.[14] The absorption coefficient K was then converted to the instrinsic absorption coefficient α according to:

$$K = 2v\alpha$$

where $v = 0.2$ is the volume fraction of Cs_2TeBr_6 in the sample.[1,14]

Solvent Properties:

Table S6. Reaction yield for the synthesis of Cs_2TeBr_6.

Metal Precursor	Solvent	Yield
$TeBr_4$	**MeCN**	51 % *
$TeBr_4$	**MeOH**	87 %
TeO_2	HBr + **MeCN**	93 %
TeO_2	HBr + **MeOH**	92 %
TeO_2	**HBr**	92 %

* Product also contained CsBr; actual yield was lower.

The reactions in the text are discussed in the context of solvent polarity and coordination strength. The quantification of these two properties is a non-trivial task, as reviewed previously in several textbooks and articles. While one may intuitively understand the chemical concept described by *e.g.* chemical polarity, a precise quantitative description is difficult, as it requires capturing many difficult electronic phenomena.

Table S7 quantifies some of these electronic phenomena using different metrics.

- Gutmann's donor number, $-\Delta H_{\mathrm{D-SbCl_5}}$ (kcal/mol), the enthalphy of formation for the adduct between an electron donor and $SbCl_5$ in a dilute solution of 1,2-dichloroethane.[15–17] Protic solvents, such as alcohols, react with $SbCl_5$ (rather than forming an adduct); as such, it is not possible to directly measure their donor numbers.
- β, a normalized value that quantifies the ability of a donor solvent to accept a hydrogen bond based on the absorption peak shifts of 4-nitroaniline.[18]
- Dielectric constant.[19,20]
- Polarity, as determined by the solvatochromic shift of the UV/vis charge transfer band of two different pyridinium N-phenolate betaine dyes dissolved in the various solvents (normalized to a reference value of 1 for water).[17]

Table S7. Properties of the solvents used in this study.

Solvent	Donor Number (kcal/mol)	β	Dielectric Constant, 25 °C	Dielectric Constant, 60 °C	Polarity
Methanol (MeOH)	-	0.615	31.5	26.0	0.762
Ethanol (EtOH)	-	0.773	24.3	19.6	0.654
Isopropanol (iPOH)	-	0.949	18.0	14.0	0.546
Acetonitrile (MeCN)	14.1	0.310	35.9	31.1	0.460
Methyl acetate (MeOAc)	16.3	0.456	6.6	-	0.253
Ethyl acetate (EtOAc)	17.1	0.446	6.0	-	0.228
Water	18.0	0.181	78.6	69.9	1

Table S8. Absorption edge contextualized in terms of various solvent properties, accounting for the 3:10 ratio of HBr (water) to organic solvent in the indicated reactions.

Metal Precursor	Solvent	Absorption Edge (eV)	β	Dielectric Constant, 25 °C	Dielectric Constant, 60 °C	Polarity
TeO_2	HBr + MeCN	2.14	0.280	44.2	38.2	0.585
$TeBr_4$	MeCN	2.17	0.310	35.9	31.1	0.460
TeO_2	HBr + MeOH	2.18	0.515	41.7	33.9	0.817
TeO_2	HBr	2.19	0.181	78.6	69.9	1
TeO_2	HBr + EtOH	2.20	0.636	34.4	27.7	0.734
$TeBr_4$	MeOH	2.20	0.615	31.5	26.0	0.762

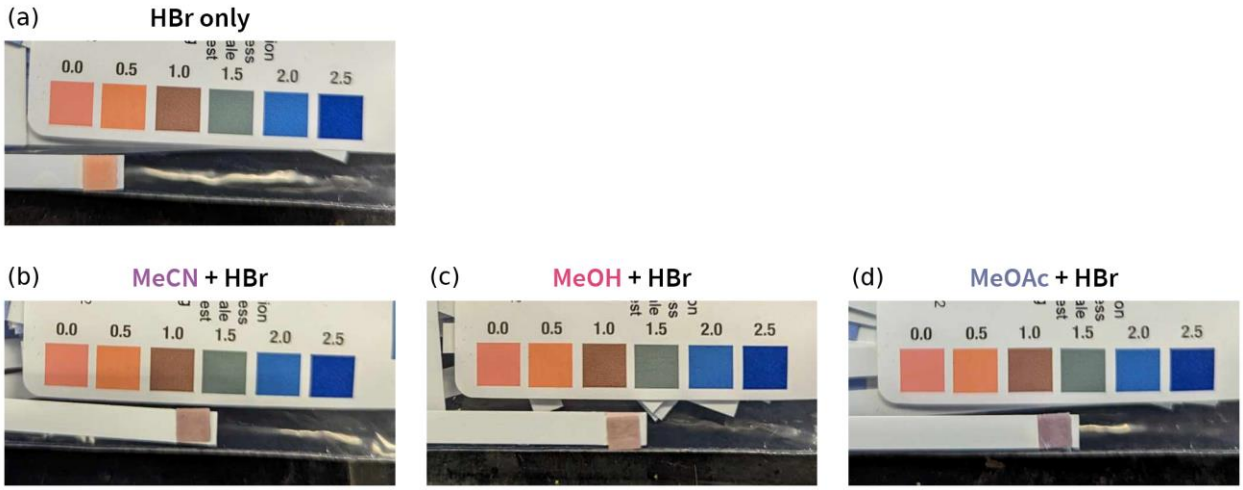

Figure S10. pH of **(a)** concentrated hydrobromic acid or mixtures of **(b)** acetonitrile, **(c)** methanol, and **(d)** methyl acetate with HBr in a 3:1 ratio.

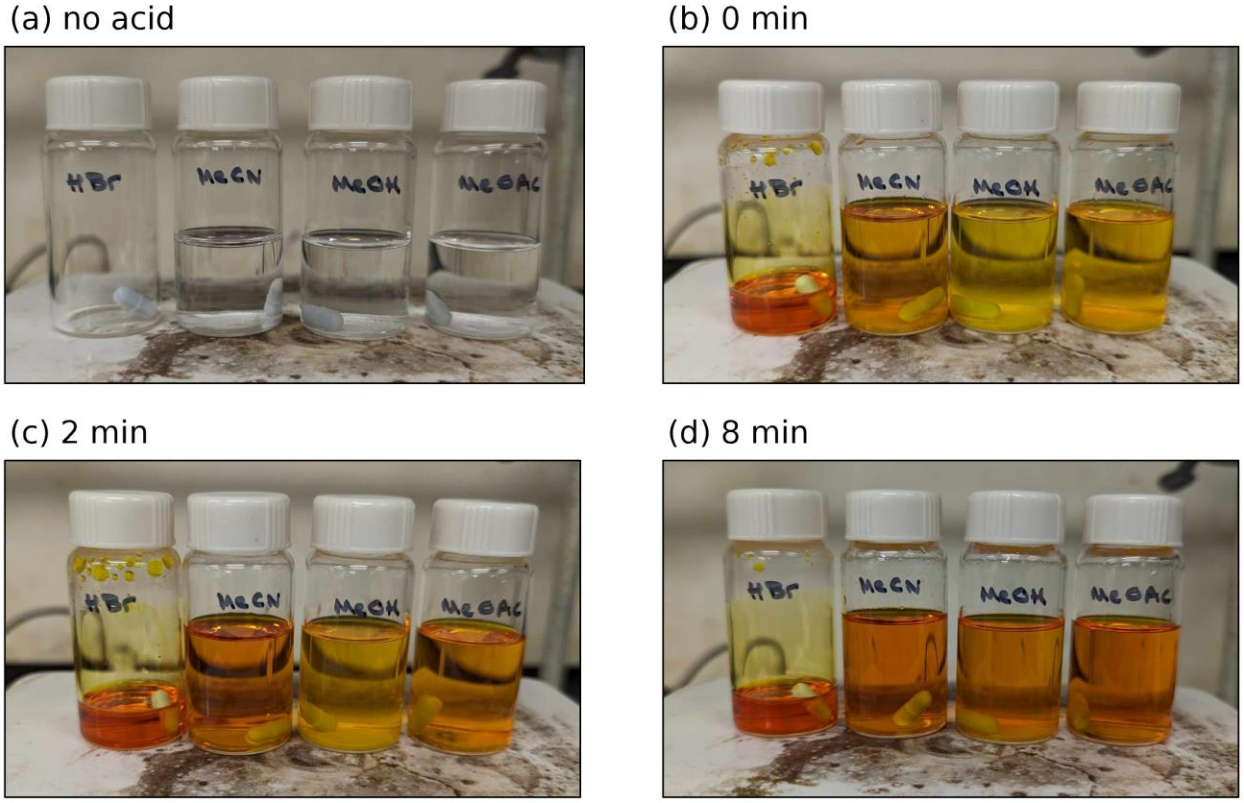

Figure S11. Progression of TeO_2 dissolution in 3 mL HBr *vs.* 10 mL MeCN, MeOH, or MeOAc with 3 mL HBr. **(a)** TeO_2 prior to the addition of HBr. The solid remains undissolved in all three organic solvents. **(b-d)** TeO_2 immediately after the addition of HBr (b) and after 2 min (c) and 8 min (d) of heating and stirring.

References

(1) Waring, R. K.; Hsu, W. Y. Urbach Rule Behavior in Strongly Absorbing Fine Particle Solids. *J. Appl. Phys.* **1983**, *54* (7), 4093–4096. https://doi.org/10.1063/1.332541.

(2) Murzin, A. O.; Samsonova, A. Yu.; Stoumpos, C. C.; Selivanov, N. I.; Emeline, A. V.; Kapitonov, Y. V. Diffuse Reflectance Spectroscopy with Dilution: A Powerful Method for Halide Perovskites Study. *Molecules* **2023**, *28* (1), 350. https://doi.org/10.3390/molecules28010350.

(3) Badger, R. M. The Relation Between the Internuclear Distances and Force Constants of Molecules and Its Application to Polyatomic Molecules. *J. Chem. Phys.* **1935**, *3* (11), 710–714. https://doi.org/10.1063/1.1749581.

(4) Kraka, E.; Zou, W.; Tao, Y. Decoding Chemical Information from Vibrational Spectroscopy Data: Local Vibrational Mode Theory. *WIREs Comput. Mol. Sci.* **2020**, *10* (5), e1480. https://doi.org/10.1002/wcms.1480.

(5) Sedakova, T. V.; Mirochnik, A. G. Luminescent and Thermochromic Properties of Tellurium(IV) Halide Complexes with Cesium. *Opt. Spectrosc.* **2016**, *120* (2), 268–273. https://doi.org/10.1134/S0030400X16020223.

(6) Li, C.-T.; Chong, M.-X.; Zhang, L.-X.; Tang, B.; Bie, L.-J. All-Inorganic Lead-Free Halide Perovskite Cs_2TeBr_6 Enables Real-Time Touchless Human Breath and Finger Related Humidity Monitoring. *Sens. Actuators B Chem.* **2023**, *379*, 133240. https://doi.org/10.1016/j.snb.2022.133240.

(7) Folgueras, M. C.; Jin, J.; Gao, M.; Quan, L. N.; Steele, J. A.; Srivastava, S.; Ross, M. B.; Zhang, R.; Seeler, F.; Schierle-Arndt, K.; Asta, M.; Yang, P. Lattice Dynamics and Optoelectronic Properties of Vacancy-Ordered Double Perovskite Cs_2TeX_6 (X = Cl^-, Br^-, I^-) Single Crystals. *J. Phys. Chem. C* **2021**, *125* (45), 25126–25139. https://doi.org/10.1021/acs.jpcc.1c08332.

(8) Huang, Q.; Tian, C.; Lai, J.; Qi, F.; Zhang, N.; Liu, J.; Liang, Z.; Wu, D.; Tang, X. Lead-Free Cs_2TeX_6 (X = Cl, Br, and I) Perovskite Microcrystals with High Stability for Efficient Photocatalytic CO_2 Reduction. *Inorg. Chem.* **2022**, *61* (36), 14447–14454. https://doi.org/10.1021/acs.inorgchem.2c02417.

(9) Peresh, E. Y.; Zubaka, O. V.; Kun, S. V.; Galagovets, I. V.; Barchii, I. E.; Sabov, M. Y. Stability Limits and Properties of Tl_2TeBr_6, Cs_2TeBr_6, and Rb_2TeBr_6. **2001**, *37* (8).

(10) Folgueras, M. C.; Louisia, S.; Jin, J.; Gao, M.; Du, A.; Fakra, S. C.; Zhang, R.; Seeler, F.; Schierle-Arndt, K.; Yang, P. Ligand-Free Processable Perovskite Semiconductor Ink. *Nano Lett.* **2021**, *21* (20), 8856–8862. https://doi.org/10.1021/acs.nanolett.1c03308.

(11) Zhu, C.; Jin, J.; Gao, M.; Oddo, A. M.; Folgueras, M. C.; Zhang, Y.; Lin, C.-K.; Yang, P. Supramolecular Assembly of Halide Perovskite Building Blocks. *J. Am. Chem. Soc.* **2022**, *144* (27), 12450–12458. https://doi.org/10.1021/jacs.2c04357.

(12) Jin, J.; Huang, H.; Chen, C.; Smith, P. W.; Folgueras, M. C.; Yu, S.; Zhang, Y.; Chen, P.-C.; Seeler, F.; Schaefer, B.; Lizandara-Pueyo, C.; Zhang, R.; Schierle-Arndt, K.; Yang, P. Benzyl Alcohol Photo-Oxidation Based on Molecular Electronic Transitions in Metal Halide Perovskites. *ACS Photonics* **2023**, acsphotonics.3c00042. https://doi.org/10.1021/acsphotonics.3c00042.

(13) Zhou, J.; Gao, B.; Wu, D.; Tian, C.; Ran, H.; Chen, W.; Huang, Q.; Zhang, W.; Qi, F.; Zhang, N.; Pu, Y.; Qiu, J.; Hu, Z.; Du, J.; Liu, Z.; Leng, Y.; Tang, X. Enhanced Photocatalytic Activity of Lead-Free Cs_2TeBr_6/g-C_3N_4 Heterojunction Photocatalyst and Its Mechanism. *Adv. Funct. Mater.* **2024**, *34* (3), 2308411. https://doi.org/10.1002/adfm.202308411.

(14) Patterson, E. M.; Shelden, C. E.; Stockton, B. H. Kubelka-Munk Optical Properties of a Barium Sulfate White Reflectance Standard. *Appl. Opt.* **1977**, *16* (3), 729. https://doi.org/10.1364/AO.16.000729.

(15) Gutmann, V. Solvent Effects on the Reactivities of Organometallic Compounds. *Coord. Chem. Rev.* **1976**, *18*, 225–255.

(16) Solute-Solvent Interactions. In *Solvents and Solvent Effects in Organic Chemistry*; Reichardt, C., Welton, T., Eds.; Wiley, 2011; pp 7–64.

(17) Empirical Parameters of Solvent Polarity. In *Solvents and Solvent Effects in Organic Chemistry*; Reichardt, C., Welton, T., Eds.; Wiley, 2011; pp 425–508.

(18) Marcus, Y. The Effectivity of Solvents as Electron Pair Donors. *J. Solut. Chem.* **1984**, *13* (9), 599–624. https://doi.org/10.1007/BF00650369.

(19) Akerlof, G. Dielectric Constants of Some Organic Solvent-Water Mixtures at Various Temperatures. *J. Am. Chem. Soc.* **1932**, *54* (11), 4125–4139. https://doi.org/10.1021/ja01350a001.

(20) Gagliardi, L. G.; Castells, C. B.; Ràfols, C.; Rosés, M.; Bosch, E. Static Dielectric Constants of Acetonitrile/Water Mixtures at Different Temperatures and Debye−Hückel *A* and a_0B Parameters for Activity Coefficients. *J. Chem. Eng. Data* **2007**, *52* (3), 1103–1107. https://doi.org/10.1021/je700055p.